IMMUNOLOGY

Septins provide microenvironment sensing and cortical actomyosin partitioning in motile amoeboid T lymphocytes

Alexander S. Zhovmer[1]*, Alexis Manning[1], Chynna Smith[2], Ashley Nguyen[1], Olivia Prince[1], Pablo J. Sáez[3], Xuefei Ma[1], Denis Tsygankov[4], Alexander X. Cartagena-Rivera[2], Niloy A. Singh[5], Rakesh K. Singh[6], Erdem D. Tabdanov[7,8]*

The all-terrain motility of lymphocytes in tissues and tissue-like gels is best described as amoeboid motility. For amoeboid motility, lymphocytes do not require specific biochemical or structural modifications to the surrounding extracellular matrix. Instead, they rely on changing shape and steric interactions with the microenvironment. However, the exact mechanism of amoeboid motility remains elusive. Here, we report that septins participate in amoeboid motility of T cells, enabling the formation of F-actin and α-actinin–rich cortical rings at the sites of cell cortex–indenting collisions with the extracellular matrix. Cortical rings compartmentalize cells into chains of spherical segments that are spatially conformed to the available lumens, forming transient "hourglass"-shaped steric locks onto the surrounding collagen fibers. The steric lock facilitates pressure-driven peristaltic propulsion of cytosolic content by individually contracting cell segments. Our results suggest that septins provide microenvironment-guided partitioning of actomyosin contractility and steric pivots required for amoeboid motility of T cells in tissue-like microenvironments.

INTRODUCTION

While amoeboid migration is likely the most typical mode of immune cell motility in tissues, the exact mechanisms underpinning amoeboid migration remain elusive to date. Recent studies have decisively determined that cell shape dynamics, cortex dynamics, and cell-environment steric interactions are the drivers of amoeboid cell motility (*1*). However, it is unclear how three-dimensional (3D) cell shape dynamics drives 3D cell locomotion, facilitating an effective cell navigation through the complex, sterically tortuous environments. For example, it is not completely understood why T cells do not require specific biochemical or structural modifications to the surrounding collagen matrix for amoeboid motility and how they rely on the active changing of cell shape and steric (i.e., nonadhesive) interactions with a collagen matrix to circumnavigate, i.e., steer around the collagen fibers, while finding available lumens for passage (*2*, *3*). Moreover, it is also not clear why the observed efficiency of amoeboid motility is proportional to the contractility of cortical actomyosin and inversely proportional to the cell-microenvironment adhesive interactions across all sterically interactive environments, such as nanotopographic surfaces, 3D collagen matrices, and cancer tumor tissue samples (*4*–*6*).

The model of amoeboid motility suggests that actomyosin contractility stimulates the formation of cell blebs, which serve as precursors for cell extension (*7*). During blebbing, the actomyosin cortex and plasma membrane serve both as a substrate for bleb formation and as a primary generator of cytoplasmic hydrostatic pressure, which causes repeating events of destabilization and transient ruptures of binding interactions between the underlying actomyosin cortex and plasma membrane (*8*–*10*). Conversely, the blebbing model of amoeboid motility does not include alternative mechanisms of nonadhesive amoeboid locomotion described for immune cells, which are the cell sliding by the retrograde cortex treadmilling in the leading bleb (*11*, *12*) and the motility by the active cortical deformation (*1*). Multiple alternative mechanisms of amoeboid locomotion described in similar cell models, i.e., migration by blebbing, sliding, and cortical deformation, suggest that all locomotion modes may represent microenvironment-specific outcomes of amoeboid cortex dynamics. The current blebbing model also does not address the spatiotemporally coordinated 3D extension of the cell cortex within a structurally discrete microenvironment, which is required for effective directional propulsion of immune cells.

Therefore, considering clinical interest, there are substantial scientific efforts aimed at improving our understanding of amoeboid locomotion in lymphocytes. We propose that studying septins can complement the current model of amoeboid motility, which depends on septins, yet via an unknown mechanism (*13*). The main challenge of studying the septin's biology is the complexity of septins. In mammals, there are 13 septin genes and at least 11 pseudogenes, coding for transcripts and proteins with extensive posttranscriptional modifications and alternative splicing isoforms (*14*). Moreover, septin's biology is very complex because septins are evolutionary old and present in divergent eukaryotic lineages, including algae and ciliates (*15*). Septins interact with multiple cellular partners, including actomyosin proteins (*16*). Previous reports show that septins participate in the formation of contractile actomyosin rings during

[1]Center for Biologics Evaluation and Research, U.S. Food and Drug Administration, Silver Spring, MD, USA. [2]Section on Mechanobiology, National Institute of Biomedical Imaging and Bioengineering, National Institutes of Health, Bethesda, MD, USA. [3]Cell Communication and Migration Laboratory, Institute of Biochemistry and Molecular Cell Biology, and Center for Experimental Medicine, University Medical Center Hamburg-Eppendorf, Hamburg, Germany. [4]Wallace H. Coulter Department of Biomedical Engineering, Georgia Institute of Technology and Emory University, Atlanta, GA, USA. [5]Department of Hematology Oncology, University of Rochester Medical Center, Rochester, NY, USA. [6]Department of Obstetrics and Gynecology, University of Rochester Medical Center, Rochester, NY, USA. [7]Department of Pharmacology, Penn State College of Medicine, The Pennsylvania State University, Hershey-Hummelstown, PA, USA. [8]Penn State Cancer Institute, Penn State College of Medicine, The Pennsylvania State University, Hershey, PA, USA.
*Corresponding author. Email: alexander.zhovmer@fda.hhs.gov (A.S.Z.); tabdanov@psu.edu (E.D.T.)

cytokinesis, indicating a possible link between septins and amoeboid migration (*13*, *17*). In particular, the septins' guanosine triphosphatase (GTPase) activity drives the assembly of major septin isoforms (i.e., SEPT2, SEPT6, SEPT7, and SEPT9) into nonpolar filaments (*18*, *19*) that stabilize actomyosin structures, such as stress fibers (*20*–*22*) and cytokinesis rings (*16*, *23*, *24*), where septins promote F-actin ring formation by cross-linking actin filaments in contractile actomyosin rings into curved bundles (*25*). It is proposed that septin-based stabilization of actomyosin structures ensures the accumulation of substantial contractile energy (*20*, *21*), which facilitates both the dynamics of the amoeboid cortex in T cells (*13*, *17*) and the cortex-driven cytokinesis (*26*). Therefore, we decide to study whether septins participate in the amoeboid motility of T cells, i.e., by regulating either actomyosin contractility or nonadhesive cell-microenvironment interactions within a structurally discrete microenvironment such as a 3D collagen gel.

Here, we show that septin GTPase activity is required for extracellular matrix (ECM)–guided assembly of F-actin and α-actinin–rich cortical rings in migrating T cells. These rings compartmentalize the contractile actomyosin cortex into peristaltic treadmilling "ball-chain" of spheroid segments. The lined-up cell segments feature hourglass topography and discrete actomyosin architecture of individual segments, which may facilitate transient steric stabilization of cells on obstacles and obstacle-evasive peristaltic translocation of cytosolic content between the adjacent cell segments. Consequently, we show that acute inhibition of septins' GTPase activity causes an abrupt loss of cell segmentation along with the obstacle-evasive 3D propulsion. Our results suggest that the amoeboid motility of immune cells within tissue-like gels is a nonstochastic 3D circumnavigation guided by the structure of a crowding microenvironment and septin-based partitioning of actomyosin contractility.

RESULTS

Human CD4$^+$ T cells subdivide cell cortex during amoeboid migration

Our principal observation is that primary human T cells (e.g., human CD4$^+$ T cell, i.e., hCD4$^+$) compartmentalize the actomyosin cortex during amoeboid migration within fibrous 3D collagen type I matrices (Fig. 1). Depending on the structural density of the surrounding collagen, migrating T cells can dynamically change their shape transitioning from a simple spheroid to complex multicameral system of interconnected spheroid compartments within the dense collagen (Fig. 1, A to C) and simple bicameral morphology within a sparse collagen (Fig. 1, D and F). Component-wise analysis of T cells segmented within the collagen matrix (Fig. 1A1) shows that during translocation of nucleus between the segments (Fig. 1, A2 and C, nucleus, arrows), nucleus is constricted by the cortex-indenting circumferential furrows identified as cortical F-actin rings (Fig. 1, A3 and B, F-actin, arrows). We also find that cortical rings are enriched with α-actinin (Fig. 2, A and B) and depleted with nonmuscle myosin 2A (NM2A) (Fig. 2C). These results suggest that heavily cross-linked cortical F-actin rings in T cells are likely similar to noncontractile and nonstretchable solid-like actomyosin structures (*27*) that mechanically stabilize the expanding cell cortex against the indenting obstacles (Fig. 2D).

The segmented morphology of migrating T cells, i.e., the lined-up segments separated by discrete F-actin rings, reminisces the septin-stabilized membranous and/or cortical rings, reported in the dividing (budding) yeasts (*28*) and some mammalian cells (*23*, *29*). Notably, we identify septins as a structural component in the leading F-actin ring in segmented T cells [e.g., septin-7; Fig. 3, A to C, +dimethyl sulfoxide (+DMSO)]. To study the role of septins in the formation of cortical rings, we proceed with inhibiting septins' GTPase activity with a recently developed mammalian septins' GTPase activity inhibitor, UR214-9 (*30*, *31*), demonstrating a similar or better inhibitory activity than a better-known fungal (i.e., yeast) septin inhibitor—forchlorfenuron (FCF). The acute chemical perturbation of septin GTPase activity causes an abrupt loss of the amoeboid organization in hCD4$^+$ T cells (Fig. 3A, +UR214-9, 40 μM, 1 hour), which manifests as (i) loss of cell segmentation, (ii) loss of cortical rings, and (iii) transition to nonmigratory morphology, characterized by the passive cell shape conformity to the surrounding collagen matrix, i.e., via elongated cell protrusions. The loss of T cell segmentation and simultaneous transitioning between the migratory (Fig. 3B and fig. S1, +DMSO) and nonmigratory phenotypes (Fig. 3B and fig. S1, +UR214-9) suggest that the hourglass-shaped cell surface formed by a cortex-indenting circumferential furrow (i.e., cortical ring) and two adjacent spheroid cell segments may actively participate in the amoeboid motility, forming steric support (fulcrum) by transiently latching the cell cortex onto confining collagen fibers (Fig. 3B, +DMSO).

For an orthogonal confirmation of septin participation in 3D amoeboid motility, we transduce mouse CD4$^+$ T cells (DO-11-10) with short hairpin RNA (shRNA) against septin-7. We target septin-7 because, unlike other septin groups, it contains only one member in all organisms, and the absence of septin-7 leads to the loss of other septin complexes (*24*). For that, the DO-11-10 cells are transfected with the small hairpin construct green fluorescent protein (GFP)–shSEP7 and then mixed with the wild-type DO-11-10 cells, labeled with Hoechst, and loaded on the 3D collagen type I fibrous matrix. The results of septin-7 knockdown shows that genetic suppression of septin-7 in DO-11-10 T cells decreases infiltration of mouse T cells in the collagen gel, compared to the wild-type DO-11-10 cells migrating within the same collagen matrices (Fig. 3D), which is consistent with data obtained using septins' GTPase activity inhibitor, UR214-9.

Amoeboid migration requires actomyosin and septin GTPase activity

To confirm the participation of septins in 3D amoeboid motility, we quantify hCD4$^+$ T cell migration in the tissue-like 3D collagen matrix (Fig. 4A) while perturbing septin's GTPase activity. As described above, static images of T cells indicate that they dynamically segment their actomyosin cortex by cortical rings during migration in 3D collagen matrices (Figs. 1 and 2 and fig. S1, +DMSO). The control T cells demonstrate treadmilling of cell segments (movie S1) and a stepwise segment-to-segment translocation of cytoplasm and nucleus through the cortical rings (movies S2 and S3 and fig. S2). Notably, septin inhibition substantially reduces the speed of migrating T cells to the near arrest (Fig. 4B, +DMSO versus +UR214-9) and substantially decreases their effective migratory displacement (Fig. 4C, +DMSO versus +UR214-9).

Previous reports indicated that actomyosin contractility is important for amoeboid dynamics in T cells (*4*, *5*). Consequently, our data confirm that contractility inhibition (+Blebbistatin, 25 μM) reduces T cell speed and displacement (Fig. 4, B and C, +DMSO versus +Blebbistatin, 1 hour), although with lower efficiency than UR214-9 (Fig. 4, B and C, +UR214-9 versus +Blebbistatin).

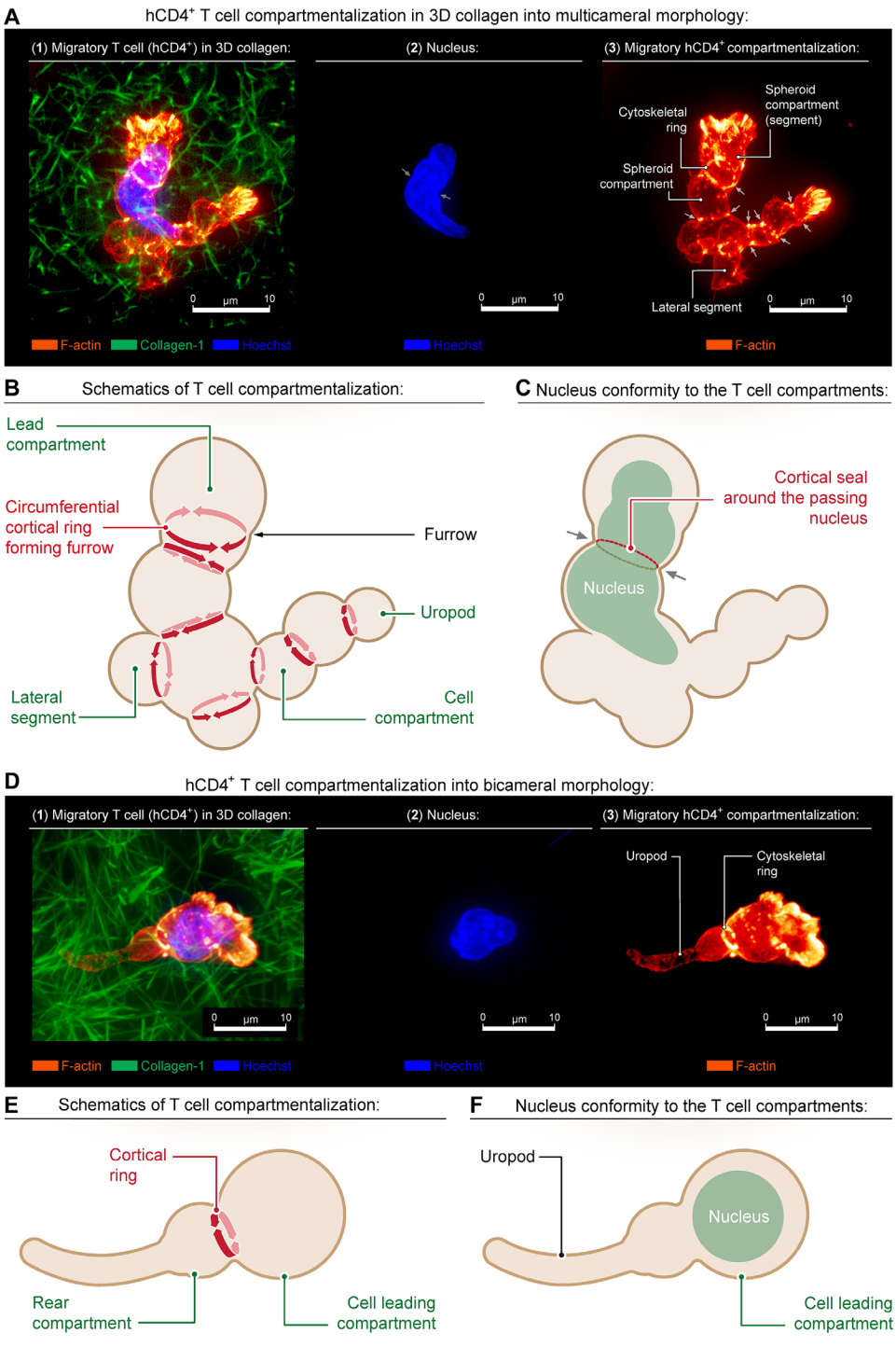

Fig. 1. Compartmentalization of T cells during amoeboid migration in collagen gels. (**A**) Compartmentalization of the human CD4$^+$ T cell cortex (i.e., hCD4$^+$, eight cortical rings) into a multicameral morphology featuring multiple spheroid segments during amoeboid migration through a fibrous 3D collagen matrix (collagen type I). Spheroid segments are separated by F-actin–enriched circumferential rings (SiR-actin staining for F-actin) that shape cortex (arrows) with the multiple circumferential furrows and indent a passing-through nucleus (arrows). (**B** and **C**) Schematic views of multicameral T cell compartmentalization. Newly formed cortical F-actin ring (circumferential furrow) separates an expanding cell segment (leading compartment) from the previously formed segments within the trailing "ball chain"–shaped cell body. (**D**) Bicameral hCD4$^+$ T cell compartmentalization (one cortical ring). (**E** and **F**) Schematic views of bicameral hCD4$^+$ T cell compartmentalization.

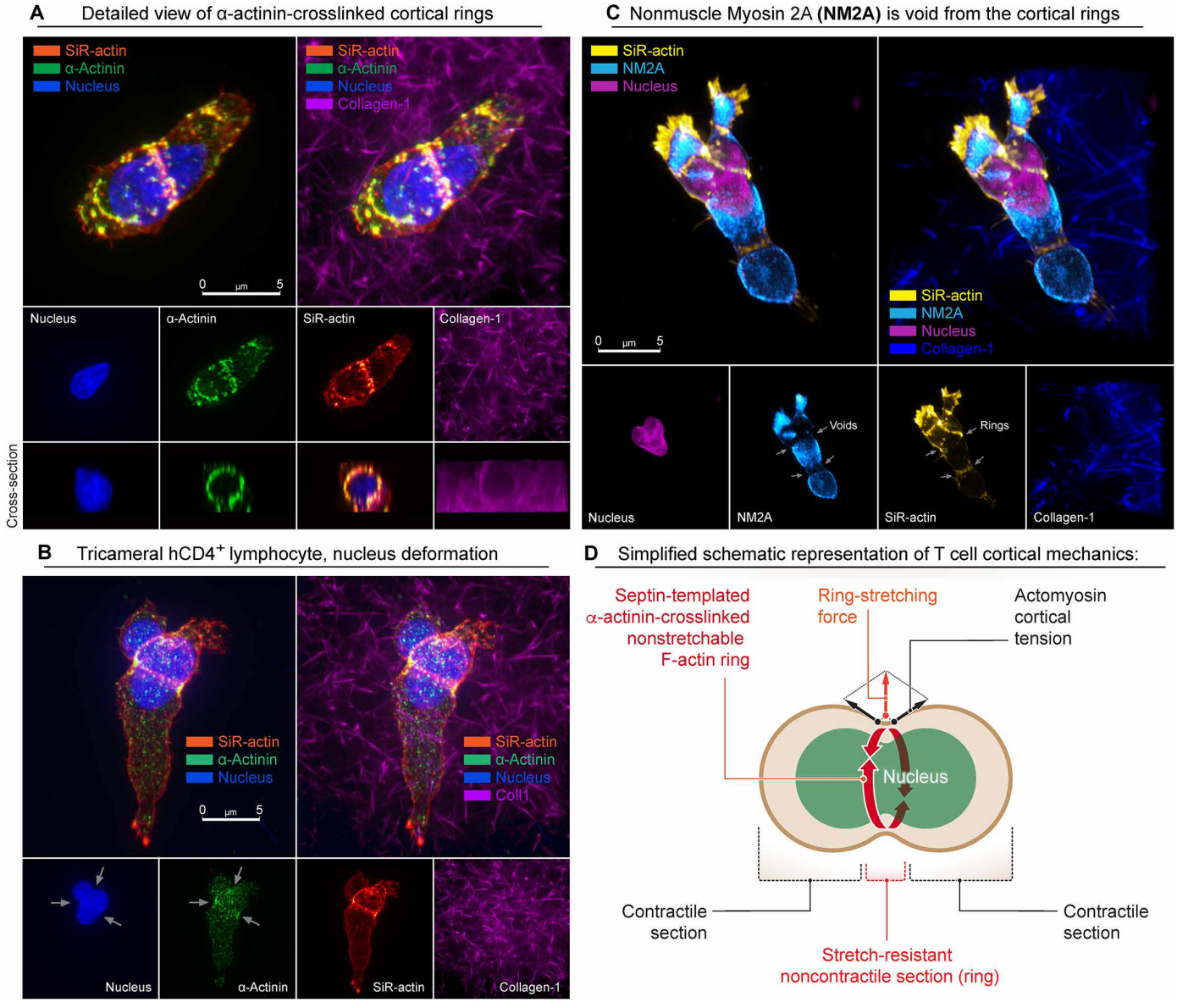

Fig. 2. Septin-templated α-actinin–crosslinked cortical rings are not contractile but provide the nonstretchable mechanics for efficient T cell cortex's compartmentalization. (**A**) Detailed view of the cortical rings reveals α-actinin as cortical rings' F-actin's cross-linker (periodic structures). (**B**) Visualization of the nonstretchable mechanics of the α-actinin–crosslinked F-actin cortical rings (nucleus deformation, arrows). (**C**) Nonmuscle myosin 2A (NM2A) is depleted from the α-actinin–crosslinked cortical F-actin rings (arrows), indicating their noncontractile yet stretch-resistant mechanics. (**D**) Schematic representation of the lymphocyte's cortical mechanics: NM2A-enriched (i.e., contractile) spheroid segments are separated by the stretch-resistant yet noncontractile α-actinin–crosslinked F-actin rings.

The stimulation of the actomyosin contractility via MT → GEF-H1 → RhoA signaling axis, achieved by microtubule depolymerization (+Nocodazole, 5 μM) (*4*, *5*, *32*), substantially increases migration speed (Fig. 4B, +Nocodazole, 1 hour) but not the effective 3D displacement (Fig. 4C, +Nocodazole) due to the reduced directionality persistence of cell migration (Fig. 4B, "diffusion exponent" and "directional ratio"). On the contrary, the activation of nondynamic actomyosin contractility, i.e., by locking actomyosin in the hypercontractile state with high tension and low dynamics, collapses T cells into immotile spheroids (Fig. 4, B and C, +Calyculin A, 50 nM, <1 hour). While our results confirm previous reports, showing that the amoeboid motility of T cells depends on the dynamic actomyosin contractility, they also demonstrate an importance of septin GTPase activity for amoeboid migration.

Septins work in conjunction with actomyosin

To test how the amoeboid motility depends on the actomyosin and septins, we apply a strategy of acute pharmacological inhibition of septin GTPase activity with UR214-9. The UR214-9 is a fluoride-derived analog of a fungal FCF septin GTPase inhibitor (*33*), but, unlike FCF, UR214-9 displays negligible cytotoxicity toward mammalian cells at high doses (*30*, *31*, *34*). In silico computation of docking

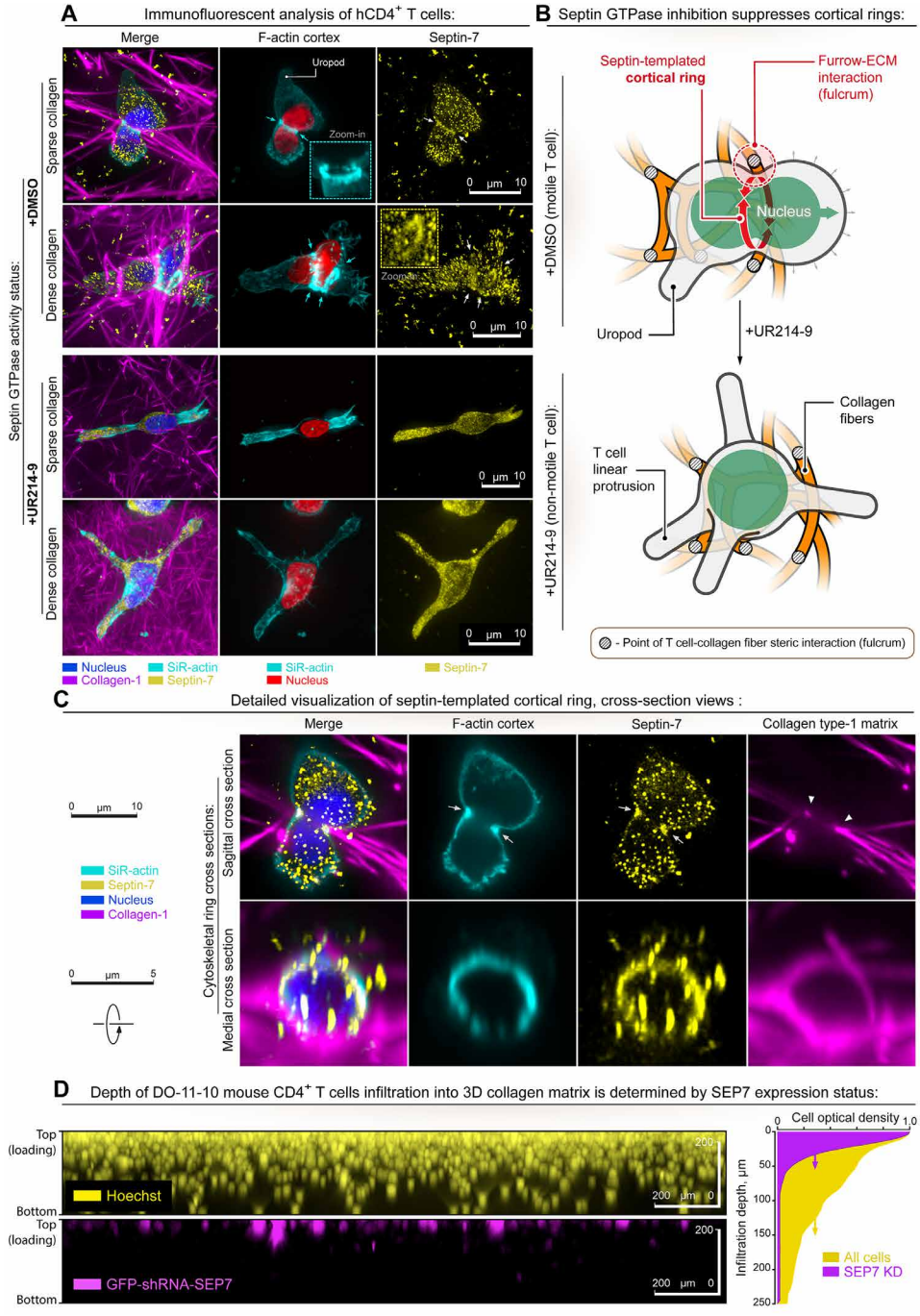

Fig. 3. Status of septin GTPase activity determines compartmentalization of T cells during migration in collagen gels. (**A**) Immunofluorescent visualization of human CD4$^+$ T cells, migrating in 3D collagen matrix: +DMSO (sparse and dense collagen)—Fixed hCD4$^+$ T cells within sparse (top row) and dense (bottom row) collagen matrices in control conditions (+DMSO). Bicameral cortex compartmentalization and a single septin-7–positive F-actin ring in sparse and multiple cortical rings (arrows) in dense collagen matrices (septin-7 immunostaining, SiR-actin). Note that in control T cells, immunofluorescence staining shows septin-7–enriched cytosolic vesicles and cortical structures. +UR214-9 (sparse and dense collagen)—hCD4$^+$ T cell loses amoeboid segmentation and the septin-positive cortical F-actin rings upon septin inhibition (+UR214-9) acquiring nonmigratory elongated cell protrusions. Note that UR214-9 also causes the loss of discrete septin-enriched cytosolic vesicles and cortical structures (as shown by a diffuse septin-7 immunofluorescence staining). (**B**) Schematics of amoeboid T cell transitions to the nonmigratory phenotype during UR214-9 treatment. Top: An amoeboid T cell forms cortical rings (sterically interactive furrows) between the adjacent spheroid compartments of larger diameters (+DMSO). During the amoeboid propulsion, collagen fiber-furrow steric interaction provides a fulcrum between the cell and 3D collagen matrix that mechanically supports peristaltic translocation of cytoplasm and nucleus without friction-loaded displacement of the entire T cell cortex. Bottom: UR214-9–mediated suppression of septin GTPase activity inhibits amoeboid segmentation (cortical F-actin ring). (**C**) Detailed medial and sagittal cross-sections of the septin-enriched (septin-7 immunofluorescence) cortical rings in the migrating T cell (see top panel). Note that the septin-positive cortical F-actin ring forms inside the confining collagen lumen (arrows). (**D**) Analysis of all nuclei positions versus GFP-positive cell positions shows a substantial loss of cell infiltration into the collagen matrix in DO-11-10 murine CD4$^+$ T cell expressing GFP-tagged septin-7–attenuating shRNA (SEP7 KD).

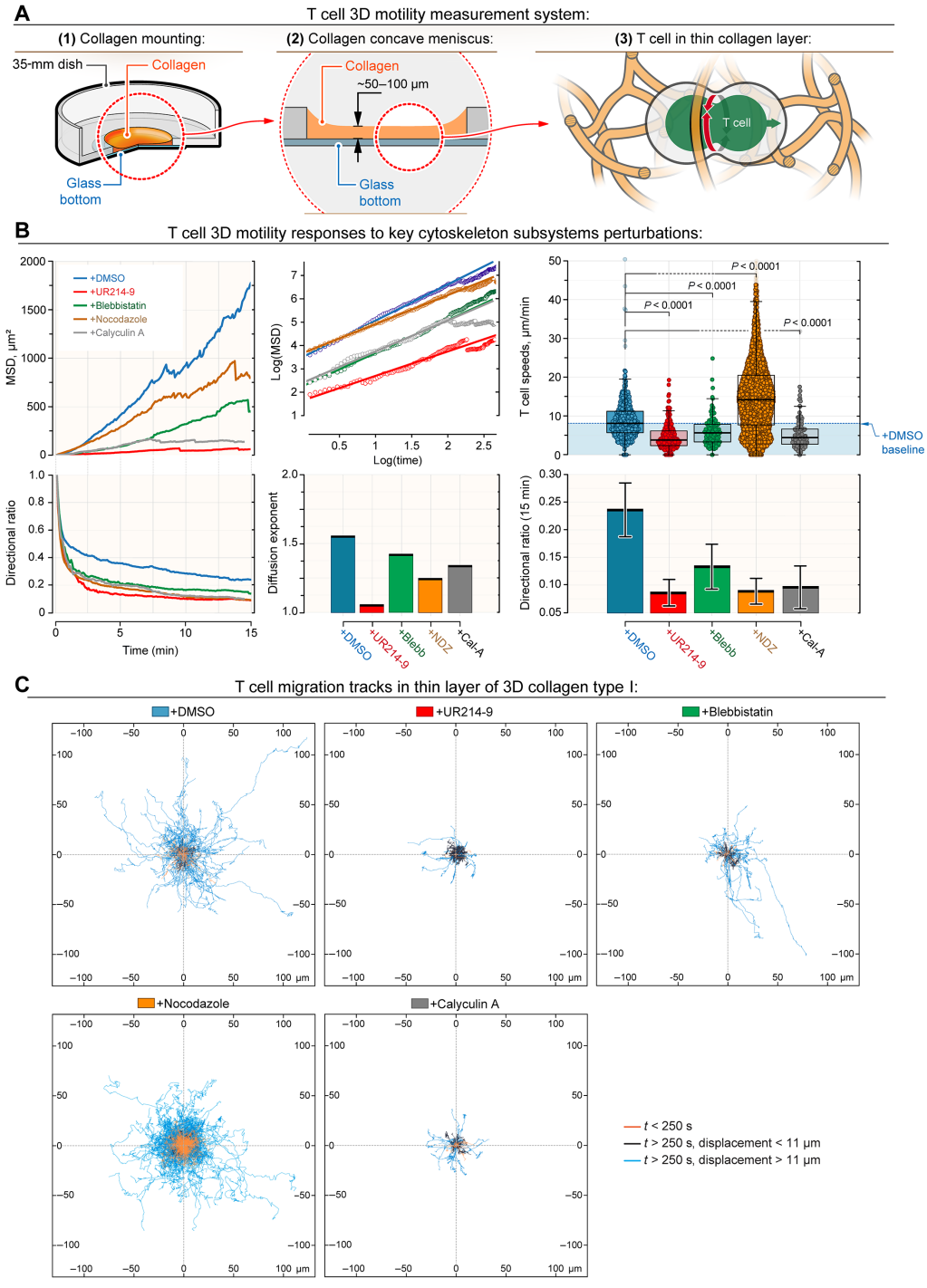

Fig. 4. Perturbation of septin GTPase activity arrests amoeboid migration of T cells within the 3D microenvironment. (**A**) Schema of live cell imaging platform (1) used for characterization of T cell migration in the 3D collagen matrix. Migrating T cells are imaged within a thin layer of collagen gel (2) and visualized in the planes positioned away from the glass (3). (**B**) Human CD4$^+$ T cells migration parameters within a 3D collagen matrix during perturbation of the key cytoskeletal subsystems: septins (+UR214-9), microtubules [+Nocodazole (+NDZ)], and nonmuscle myosin contractility [+Blebbistatin (+Blebb) and +Calyculin A (+Cal-A)]. Note that mean velocity values of automatically detected and tracked T cells do not reach zero due to the lack of sufficient T cell–collagen adhesion. Insufficient adhesion enables lymphocytes' passive oscillations (e.g., Brownian motion) within a 3D collagen matrix, which includes completely arrested T cells (e.g., +UR214-9 or +Calyculin A treatments). Passive T cell oscillations do not result in the lymphocyte's persistent displacement within the collagen matrix. MSD, mean square displacement is the population-wide average of the squared values of the linear distance between the T cell position at time t and its initial position on the track ($t = 0$). Displacement ratio is the population-wide average value of the ratios of the linear distance between the T cell position at time t and its initial position on the track to the distance that T cell has traveled along its curved track up to time t. (**C**) 2D projections of the human CD4$^+$ T cell migration tracks within a thin layer of 3D collagen matrix during perturbation of the key cytoskeletal subsystems. Note that both +UR214-9 and +Calyculin A treatments induce potent arrest of T cell displacement, due to the complete loss of amoeboid cortical dynamics.

configurations to septin-7 dimer for guanosine diphosphate, UR214-9, and FCF indicates similar or better inhibitory activity of UR214-9 compared to FCF (fig. S3, A to D). Moreover, analysis of septin complexes by native gel electrophoresis shows that inhibition of septin GTPase activity with UR214-9 leads to the loss of other septin complexes (fig. S3, E and F).

To test that UR214-9 functions like FCF, i.e., provides an abrupt and detectable loss of septin-actomyosin interactions (*20*, *21*, *23*, *35*, *36*), we choose the mesenchymal triple-negative adenocarcinoma MDA-MB-231 cell line. Compared to T cells, MDA-MB-231 cells feature distinct contractile actomyosin structures, i.e., stress fibers. Using imaging of stress fibers, we visualize that acute inhibition of septin GTPase activity (+UR214-9) results in rapid translocation of septins (e.g., endogenous septin-9, immunofluorescent analysis) from the stress fibers to the cytosol (fig. S4A, +DMSO versus +UR214-9). Rapid translocation of septins is accompanied by the structural dissolution of stress fibers resulting in partial cell retraction and detachment (fig. S4A, +UR214-9, 40 μM, 1 hour). Similarly, in live cells transfected with GFP–septin-9, the collapse and disintegration of septin-positive filaments into the curled fragments (fig. S4B, +DMSO, +UR214-9, 1 hour) occur during the first hour after the addition of UR214-9.

In the orthogonal experiment with MDA-MB-231 cells, we suppress actomyosin contractility by targeted myosin II inhibition with blebbistatin, which results in a similar collapse of the stress fibers decorated with septin-9, as shown by fragmentation and redistribution of GFP–septin-9 filaments that are no longer associated with stress fibers (fig. S4C, +Blebbistatin, 50 μM, 1 hour). These experiments are consistent with the hypothesis that the fluoride-derived FCF analog UR214-9 acts like FCF, causing the loss of septin-actomyosin interactions. Moreover, our data suggest that septins and contractile actomyosin structures are mutually interdependent, i.e., septins stabilize the tensile actomyosin, while loss of myosin-driven F-actin contractility destabilizes the associated septin structures, supporting previous findings that homozygous loss of septin-9 in mouse embryonic fibroblasts causes a loss of stress fibers and associated septin filaments (*37*).

Septins provide sensing of cortex-indenting obstacles

To study the role of septin-actomyosin interactions in 3D motility, we analyze where T cells typically feature septin-enriched cortical rings. We note that these rings are found exclusively at the cell surface sites indented by collagen fibers (Fig. 5A, arrows). The formation of cortical rings at the indentation sites (Fig. 5B) indicates cell compartmentalization and conformational adaptation (Fig. 5C) in response to the complex configuration of the surrounding obstacles (Fig. 5D), allowing for the peristaltic translocation of the cytoplasm and nucleus along the sequence series of the resulting cell segments.

Analysis shows that control T cells (+DMSO) have an average of two to three rings per cell (Fig. 5B, left), and no cortical rings are observed without a cell surface–indenting contact with collagen fibers (Fig. 5B, right). Immunofluorescent analysis of spatial colocalization and cross-correlation for the cellular components of cortical rings and cell surface–indenting collagen fibers shows stereotypical architecture of F-actin and septin-7 structures on collagen fibers (Fig. 6, A to D, and movie S4). For all cells analyzed, the median offset between indenting collagen and cortical rings is 0.22 μm, highlighting the consistent asymmetry between maximal intensities of the F-actin and collagen signal distributions along the direction of the ring axis (Fig. 6E). The F-actin distribution is shifted toward the direction of the protruding part of the cell. The shift between F-actin and septin-7 is at the borderline of the image resolution (0.065 μm), indicating a strong (nearly perfect) overlap of F-actin and septin-7 distributions at the ring.

From the mechanistic standpoint, septins are well-known sensors of the plasma membrane curvatures (i.e., second-order surface curves) that preferentially assemble into isotropic networks on the inside of spheroid (convex) surfaces (Fig. 7, A and B), avoid concave surfaces, and self-organize into the macroscopic fibers along the spine of the indenting furrow on the inside (mixed, i.e., saddle) surfaces of the cell membrane (Fig. 7, C and D) (*38*). For example, we observe curvature-sensitive accumulation of septin-7 (SEP7-GFP) filaments along the convex cortical ridge at the foot of the paranuclear dome in the MDA-MB-231 cells (Fig. 7, A and B, and fig. S5).

Thus, a possible scenario of septin-7 assembly is that in T cells, collagen fibers, by crowding interactions with the membranes of migrating T cells (*3*), create cortex-indenting mechanical collisions between the cell cortex and surrounding ECM obstacles with a curvature that is sufficient to trigger the local assembly of septins (Fig. 5C). Our observations also indicate that curvature-guided septin assembly may happen across various types of immune cells. For example, natural killer NK-92 lymphocytes compartmentalize cortex in collagen gels (Fig. 8, A to C) and condense septin fibers along the collagen fiber–induced cortex indentations (Fig. 7C, arrows). Similarly, NK-92 lymphocytes, passing through 5-μm plastic pores, form the septin-7–rich and F-actin–dense circular structures (Fig. 7D), resembling cortical rings and septin-mediated plant invasion structures described for fungi (*39*).

Septins compartmentalize actomyosin contractility for circumnavigation

For T cells and other lymphocytes, the microenvironment-guided cell compartmentalization was previously unrecognized. Structurally, this cell compartmentalization by cortex-indenting collagen fiber manifests as a sterically interactive furrow marked by the assembly of a septin-enriched cortical ring (Fig. 9A). We propose that the "segment-ring-segment" topographic unit of gel-invading T cell mechanically latches its cortex on collagen and serves as a nonadhesive, i.e., steric, fulcrum that facilitates peristaltic translocation of the nucleus and cytosolic content into the newly formed invading cell segment (Fig. 9B). This stepwise peristaltic translocation of the nucleus and cytosolic content along the treadmilling chain of forming and shrinking T cell segments would require spatiotemporally coordinated contractility of the actomyosin cortex to provide directed cytosolic hydrostatic pressure (*20*, *36*). Immunofluorescence analysis of segmented T cells reveals an uneven spatial distribution of activated phosphorylated (Ser^{19}) myosin across adjacent cell cortical segments (Fig. 9C1 and fig. S6). The differential density of activated cortical actomyosin between individual segments (Fig. 9C2) indicates that each cell segment can feature an individual level of cortical contractility required for spatiotemporally coordinated peristaltic dynamics of the entire cell cortex (Fig. 9, D and E).

Our immunofluorescence data also align with the live dynamics of translocation of cytosol and nucleus across multiple segments during 3D migration of T cells in the collagen matrix (movies S1 to S3 and fig. S2). In particular, we observe that each locomotion cycle in a migrating T cell includes propulsion of cytosol and nucleus and initiation of a new cell segment. The "old" or used cortical segments,

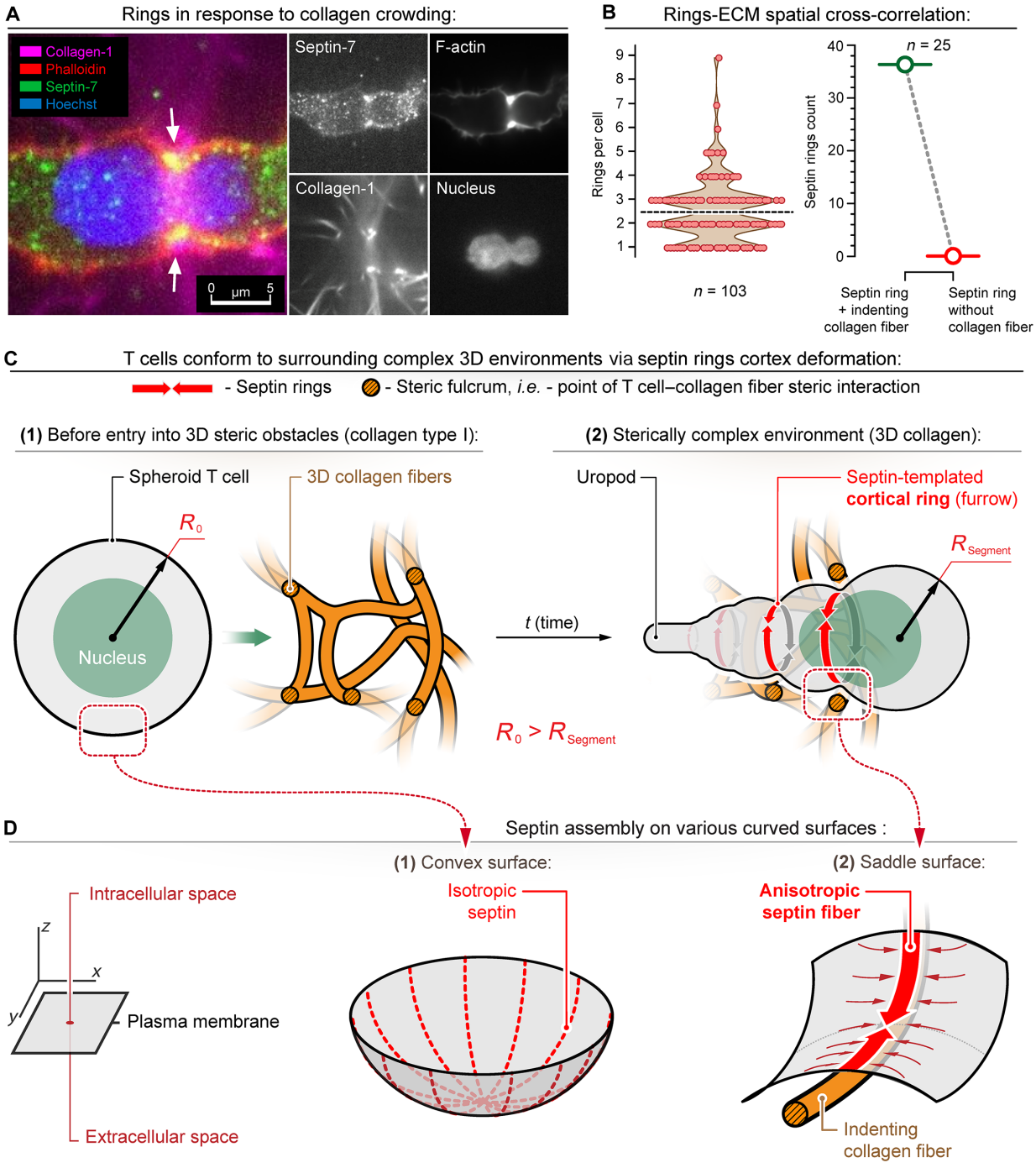

Fig. 5. 3D structure of the extracellular matrix guides the formation of septin-positive cortical rings. (**A**) Sagittal cross section of the amoeboid T cell migrating through the 3D collagen matrix. Note that the septin-positive (septin-7) cortical ring forms at the site of the T cell mechanical interaction (cell surface–indenting) with the collagen fibers (arrows). (**B**) Immunofluorescent analysis of spatial colocalization and cross-correlation for the cortical rings and cell surface–indenting collagen fibers. Left: Distribution of the rings-per-cell counts (mean value ~2.5 ring per cell, dashed line). Right: Cortical rings are linked to the presence of cell surface–indenting ECM (collagen) fibers. Note that rings are always associated with the adjacent collagen fiber (ring + collagen), while there is no identified T cell ring without the presence of a T cell–indenting collagen fiber. (**C**) Schematic representation of the ECM-induced T cell transitioning from the nonmigratory spheroid to the migratory compartmentalized architecture during its amoeboid migration through the sterically interactive 3D collagen gel. External 3D topography of collagen fiber meshwork surrounding an initially spheroid T cell (1) provides a guiding spatial configuration of the steric and mechanical pressure stimuli, to initiate a series of septin-driven T cell compartmentalization events (2) required for amoeboid migration. Note that the resulting T cell's segment radii ($R_{Segment}$) are smaller than the radius (R_0) of the spheroid T cell. (**D**) Schematic representation of septin assembly on the inner side of the T cell plasma membrane surfaces with various curvatures. (1) Isotropic assembly of septin filaments on convex surface, e.g., in a spheroid cell. (2) Anisotropic assembly of septins on the saddle surface formed by a cell surface–indenting collagen fiber, e.g., initiation of the assembly of the compartmentalizing septin rings in a migrating T cell in response to the external obstacles.

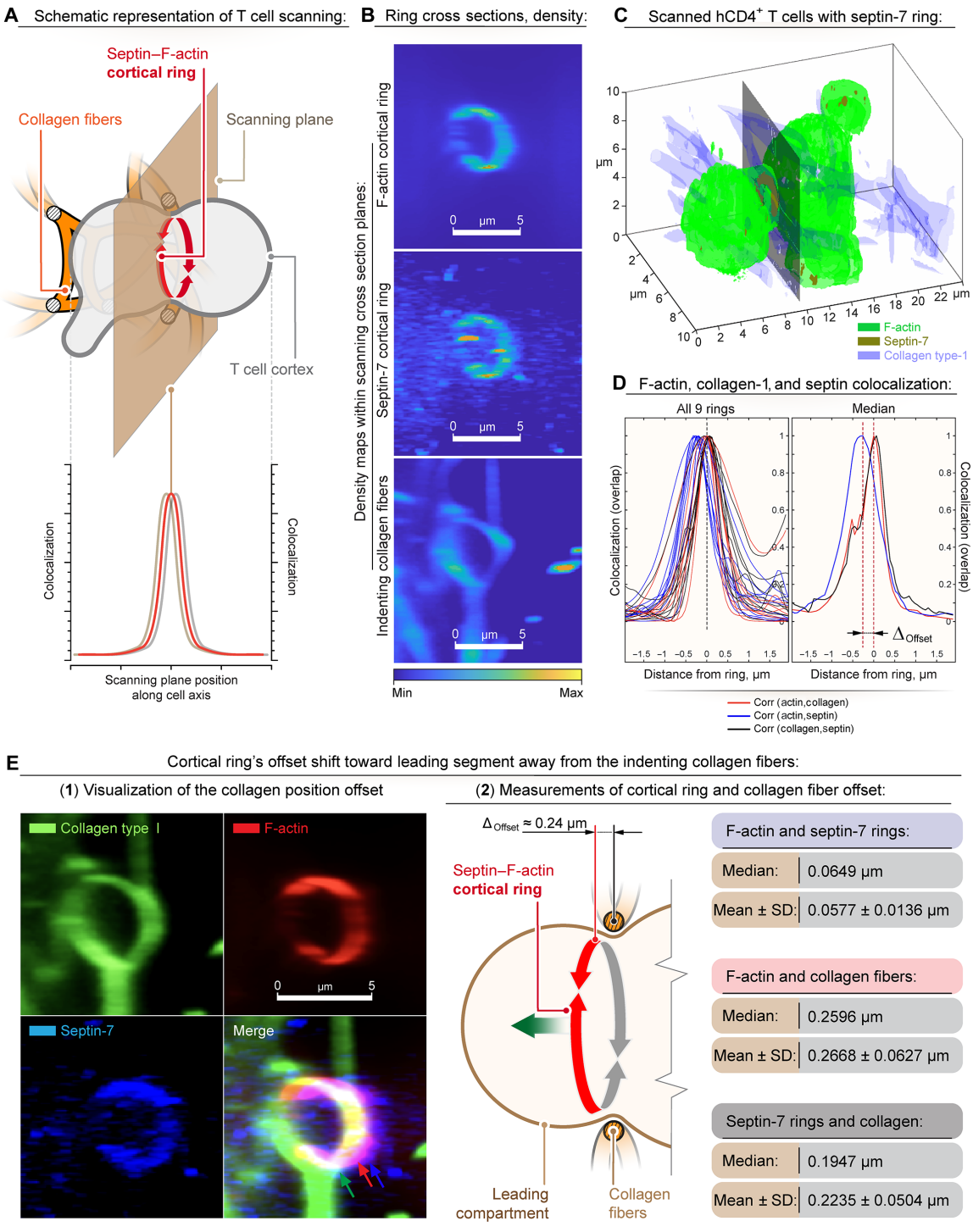

Fig. 6. Immunofluorescent analysis of spatial colocalization and cross-correlation for the cellular components of cortical rings and cell surface–indenting collagen fibers in hCD4$^+$ T cell. (**A**) Schema of the scanning through the T cell with ECM-induced cortical ring. The orientation of the scanning plane is aligned with the plane of the cortical ring. (**B**) Fluorescent signals from F-actin, septin-7, and collagen channels in the cross section of the scanning plane at the position of maximal F-actin intensity. (**C**) 3D surface reconstruction of the z-stack data (movie S4). Green, F-actin low-threshold channel represents the whole cell shape; red, F-actin high-threshold channel and defines the cortical ring; blue, collagen channel represents the collagen fiber matrix surrounding the cell. (**D**) Left: F-actin–collagen overlap (red), F-actin–septin-7 overlap (blue), and collagen–septin-7 overlap (black) for nine individually analyzed cortical rings. Right: Median overlap curves. All curves are normalized to 1, centered by the peak of the red one (overlap of F-actin and collagen). The distance between the peaks of black and blue curves, Δ_{Offset}, represents the shift between the maximal intensity planes of the F-actin and collagen rings. (**E**) (1) F-actin, septin-7, and collagen signals in the planes of maximal intensity and the merged channel show a strong overlap of the three signals in the view of the ring plane despite the shift Δ_{Offset} in the perpendicular (ring axis) direction. (2) Schematic representation and calculated values of the cortical ring offset shown in (D) highlighting the asymmetry between maximal intensities of the F-actin and collagen signal distributions along the direction of the ring axis.

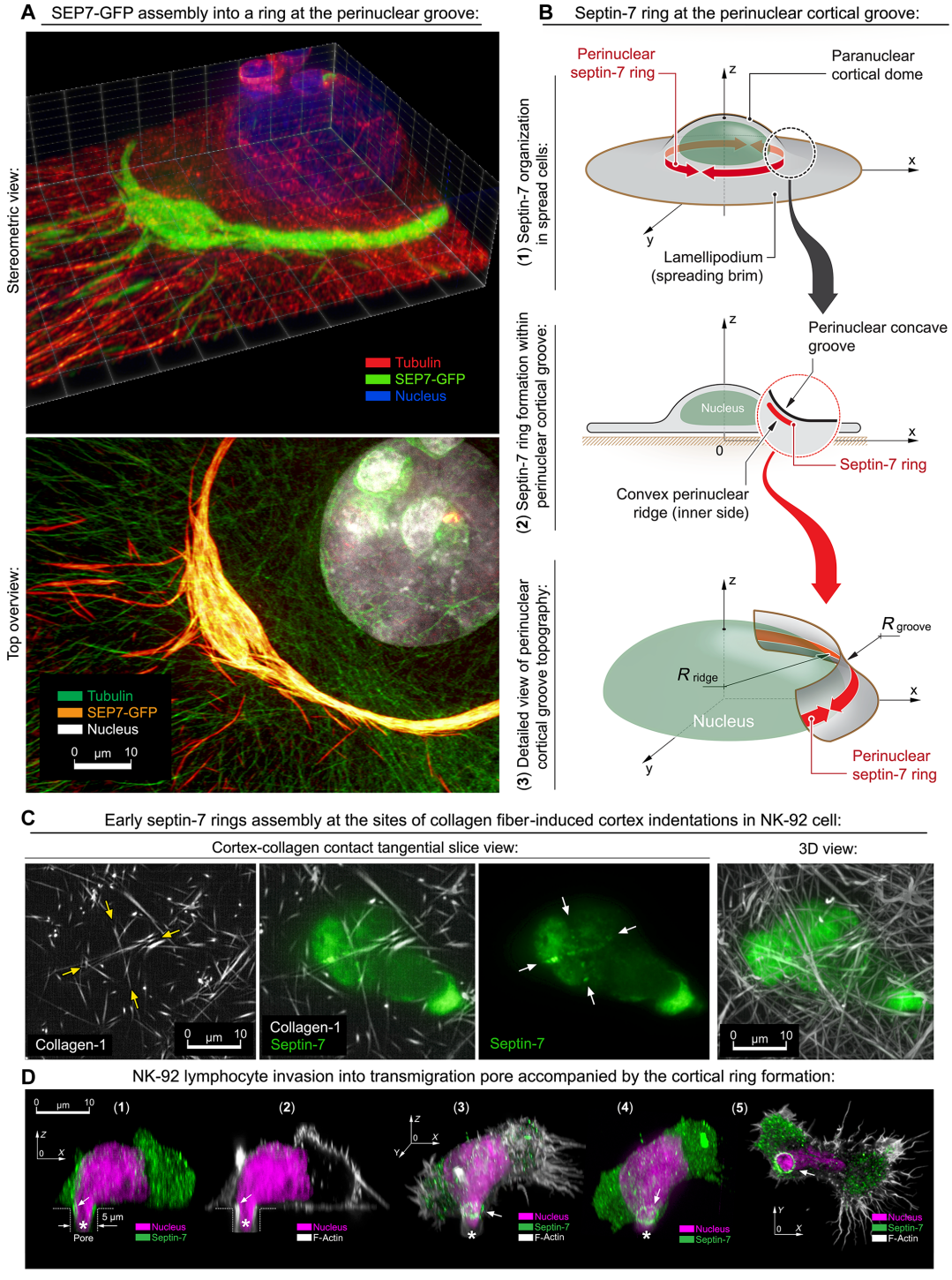

Fig. 7. Membrane (cortex) curvature-sensitive accumulation of septin-7 (SEP7-GFP) filaments at the inner side of deflection, i.e., along the convex ridge in the MDA-MB-231 cells or collagen fiber–induced indentation in NK-92 lymphocytes. (**A**) Detailed iSIM microscopy view of the perinuclear region that features a deflection of the cell cortex/plasma membrane surface around the nucleus-induced cell dome, i.e., perinuclear concave groove (convex ridge on the inner side of the cortex). Note a selective accumulation of the SEP7-GFP filaments at deflection regions of the cell plasma membrane and cortex. (**B**) Schematic representation of curvo-sensitive behavior of SEP7-GFP, forming the filaments aligned along the convex ridge at the perinuclear region. (**C**) Tangential slice views of the amoeboid NK cell (NK-92 cell line) migrating through the collagen matrix. Early stage of septin-7 assembly (septin-7 immunofluorescence, green) into the cortical ring starts at the sites of T cell surface indentation, caused by the T cell pressure against the collagen fibers (arrows). (**D**) 3D views of an NK-92 lymphocyte entering the 5-μm transmigration pore (dashed lines) with an invading segment (asterisk). (1 and 2) Sagittal cross-sectional view indicates assembly of septin-7 (1) and F-actin (2) dense cortical structure at the entrance into the pore (arrows). (3) Stereometric 3D views of the NK-92 cell show a complete and mature cortical ring (arrow). (4) Detailed septin-7 ring view (arrow) at the neck of the invading segment. (5) View from the bottom at the invading protrusion (arrow) NK-92 cells.

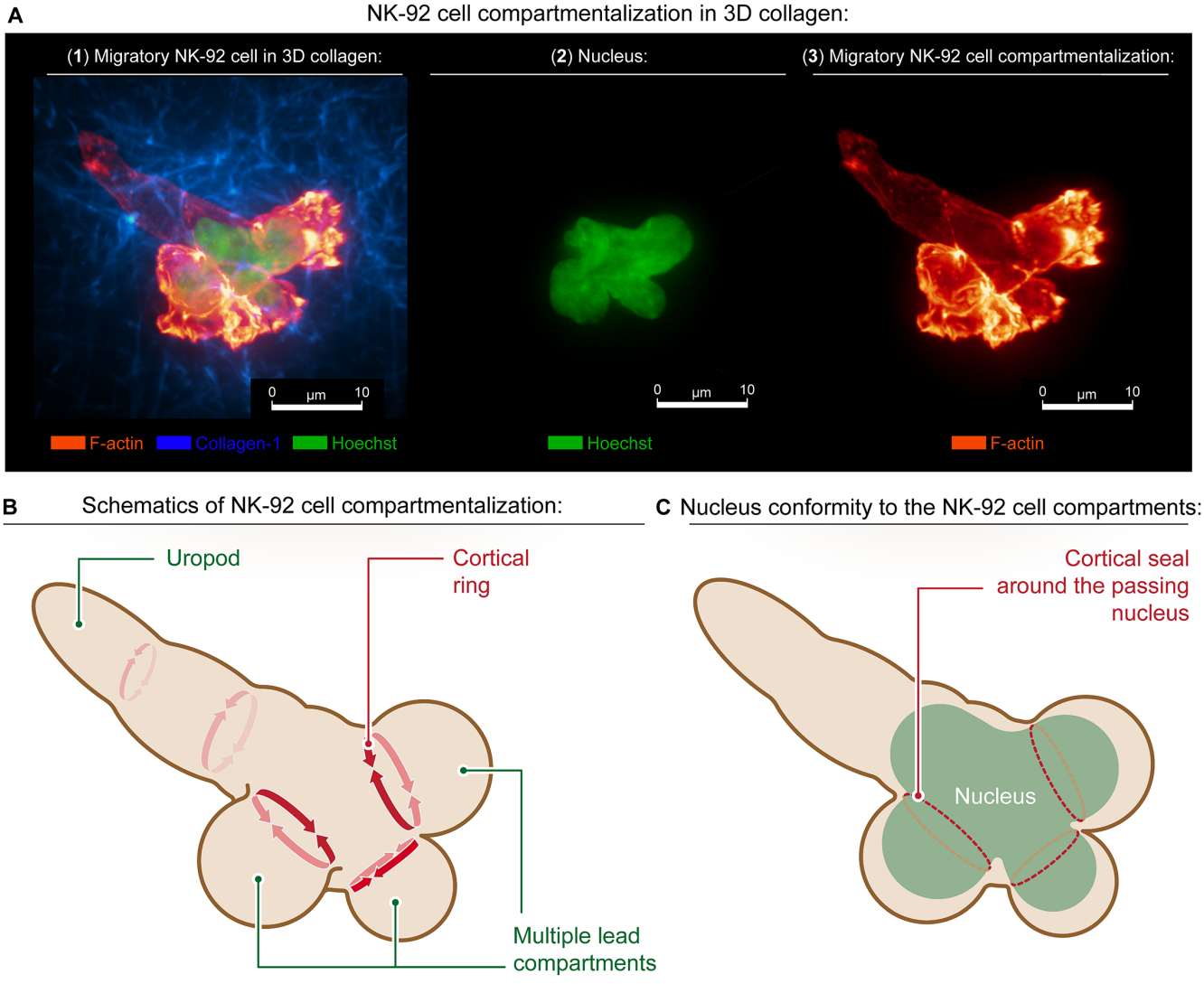

Fig. 8. Compartmentalization of NK-92 cells during amoeboid migration through collagen gels. (**A**) Compartmentalization of the NK-92 cell cortex into multiple spheroid segments during amoeboid migration through a fibrous 3D collagen matrix (collagen type I). Spheroid segments are separated by F-actin–enriched circumferential rings (SiR-actin staining for F-actin) that shape cortex with the multiple circumferential furrows and indent a passing-through nucleus. (**B** and **C**) Schematics of NK-92 compartmentalization displays multiple leading segments (leading compartments) that share nucleus via its protruding lobules.

which are located behind the nucleus, undergo gradual degradation, recycling, and compaction, manifesting as the rear-located cylindrically shaped uropod (Fig. 9, F and G).

In the orthogonal live imaging experiment with GFP-NM2A mouse $CD4^+$ T cells, we also observe compartmentalized dynamics of actomyosin cortex during amoeboid migration throughout 3D collagen matrix (Fig. 10 and movie S5). Specifically, our data indicate spatiotemporal correlation between density of cortical myosin and the peristaltic contraction-expansion dynamics of the T cell compartments (Fig. 10A and movie S6). Moreover, the spatiotemporal superposition (maximum projection) of the peristaltic events highlights zones of myosin depletion at the typical sites of the intersegmental cortical rings (Fig. 10B). In addition, dynamics of myosin cortical density is synchronized with migratory peristaltic events (Fig. 10C and movie S6) and shows that the myosin's intensity peaks are in the antiphase with the myosin half-maximum area, indicating that the local cortex's contraction is proportional to the locally accumulated myosin.

On the basis of these data and the existing model for the stochastic cortical instability as a driving force of amoeboid motility (*40*), we suggest a model of steric guidance, which is a nonstochastic cortical partitioning in amoeboid cells driven by ECM structure. Specifically, we suggest that the mechanical collision between the expanding cell segment and the confining steric obstacles creates cortical indentation, which may trigger septin condensation and assembly of a new cortical ring followed by the separation of a new cell segment. The treadmilling of ECM-conformed cell segments provides lymphocytes with a circumnavigating mechanism for a stepwise obstacle-avoiding peristaltic translocation of cytosol and nucleus between cell segments (Fig. 9E).

For a complex tissue-like environment, e.g., collagen matrix, such stepwise ECM-guided peristaltic motility manifests as circumnavigation,

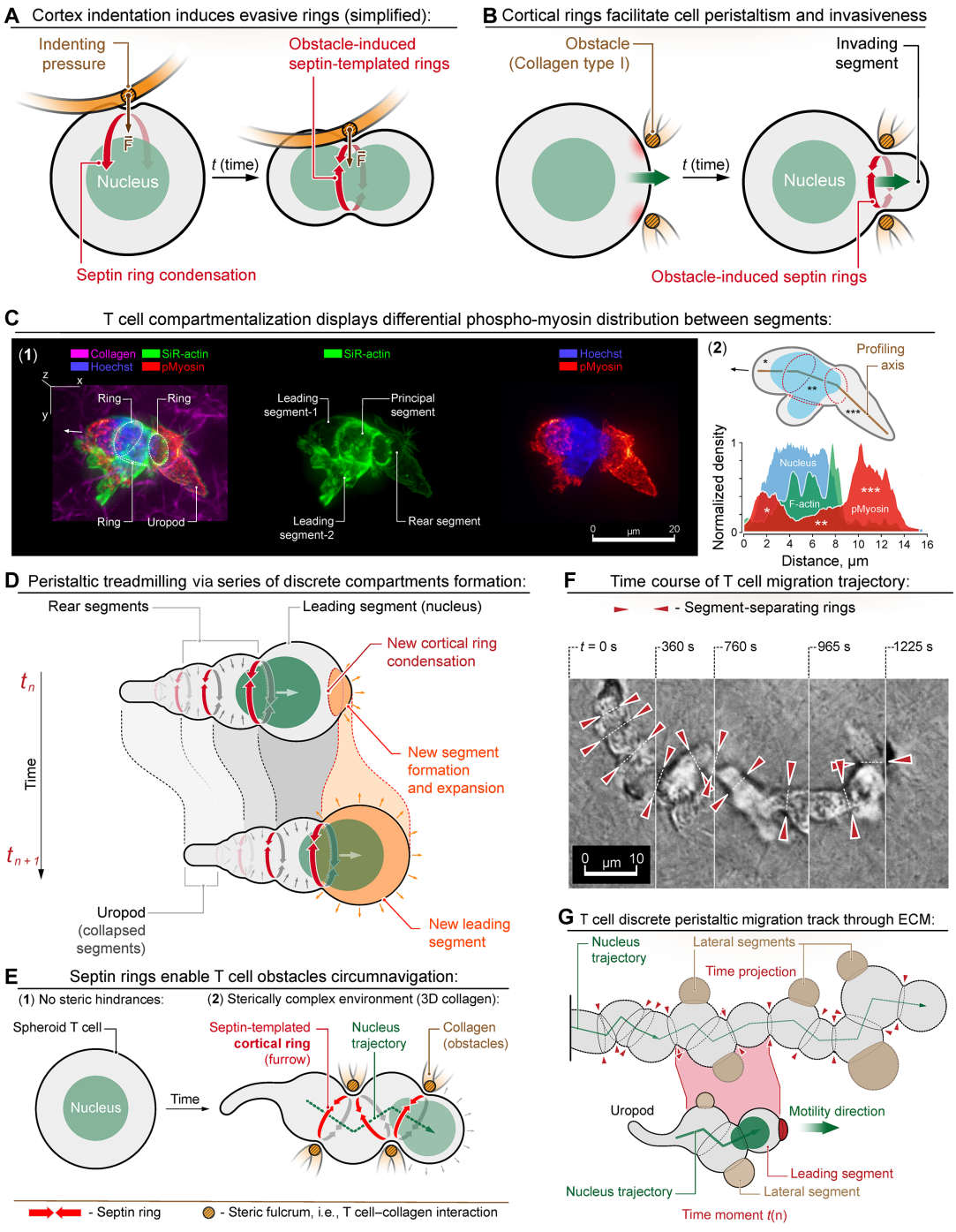

Fig. 9. Actomyosin cortex compartmentalization by localized formation of the septin rings in response to the external obstacles enables T cell peristaltic circumnavigation within complex 3D microenvironments. (**A**) Schema of evasive cell surface deformation into cortical rings. Deformation is initiated by cell surface–indenting collagen fibers. The resulting furrow forms a transient steric lock, i.e., fulcrum, onto indenting collagen fibers. (**B**) Schema of adhesion-independent invasive amoeboid propulsion. Collagen-induced cell partitioning initiates a stepwise peristaltic translocation of cytosolic content into the invading cell segment without friction-loaded displacement of the entire T cell cortex. (**C**) (1) 3D view of the hCD4^{+} T cell (+DMSO) in the collagen matrix with multiple rings and discrete segments. The cortex in adjacent segments displays a differential density of phospho-myosin [phospho-myosin light chain 2 (Ser^{19}) immunofluorescence]. (2) Cumulative density profiling for phospho-myosin light chain 2, F-actin, and chromatin along the T cell's main axis, i.e., across the principal segments. (**D**) Schema of amoeboid T cell locomotion by peristaltic treadmilling of discrete cell segments. Series of the new compartments formation at the leading front of the cell is accompanied by the nucleus and cytosol translocation (movies S1 to S3). (**E**) Schematic representation of T cell amoeboid circumnavigation through 3D collagen: Fiber-induced septin rings deform the T cell cortex to conform to the surrounding obstacles, allowing T cells to efficiently treadmill around and between the structurally complex collagen matrix. (**F** and **G**) Time course superposition (F) and a schematic representation (G) of the single hCD4^{+} T cell highlighting migration track within the 3D collagen matrix. The T cell's nucleus trajectory is a zigzag track between the chambers through cortical rings (arrowheads).

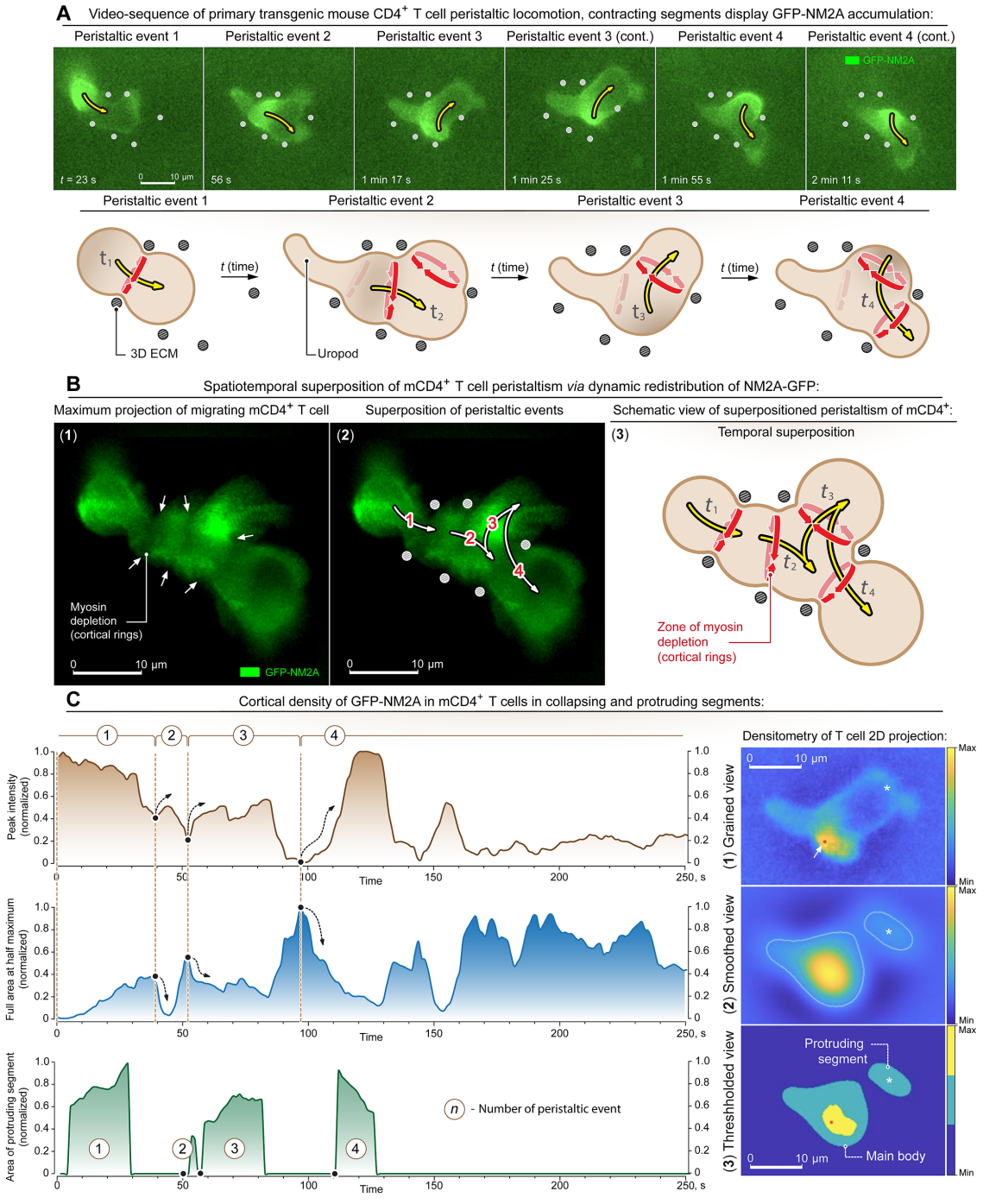

Fig. 10. Live dynamics of cortical NM2A in the distinct cell segments during amoeboid migration. (**A**) Video sequence (top, movie S5) and schema (bottom) of amoeboid migration of the primary GFP-NM2A-transgenic mouse CD4$^+$ T cell throughout the 3D collagen matrix. Peristaltic cytoplasm translocation is shown with arrows. (**B**) Spatiotemporal superposition (maximum projection) of the peristaltic events, shown in (A). (1) Maximum intensity projection of GFP-NM2A highlights myosin-depleted belts between T cell segments (arrows), i.e., at typical positions of the intersegmental cortical rings. (2) Schema of the peristaltic event superposition (numerated) defines the path of T cell amoeboid peristaltic movement. (3) Combined schema of the T cell's peristaltic events and cortical architecture superpositions (rings and segments). (**C**) Dynamics of the myosin cortical density is synchronized with peristaltic events and T cell 3D amoeboid motility (movie S6). Left: Normalized intensity values of the peak myosin density (top), cell area with myosin optical densities above its half maximum value (middle), and area of the newly protruding segments (bottom). Right: Densitometry of the GFP-NM2A signal in mCD4$^+$ T cell (peristaltic event 3): Grained (1), smoothed (2), and thresholded (3) views of the myosin density. (3) Thresholded view highlights a newly forming protruding T cell's segment. Red dot, maximal myosin density (white arrow). White asterisk, geometric center of the protruding segment defined in (3). The dynamics of myosin's peak intensity is in the antiphase with the half-maximum area (ascending and descending black arrows) indicating that the local cortex' contraction is proportional to the locally accumulated myosin. The dynamics of the maximal intensity and the area of the protruding bleb are in phase. Position of the peak intensity is always in opposition to the newly protruding segment.

i.e., the obstacle-evasive zigzag-like trajectory of amoeboid cells. Notably, live imaging of the multi-segmented hCD4$^+$ T cells within the 3D collagen matrix shows that lymphocytes repeatedly form a zigzagging trajectory (Fig. 9, F and G, and movie S1), emphasizing the migration path between and around collagen fibers through the available lumens (i.e., circumnavigation). During circumnavigation, T cells continually treadmill old shrinking and newly formed expanding discrete cortical segments formed in response to cell surface–indenting steric obstacles (Fig. 9G).

DISCUSSION

The structural and migration signatures of septins in immune cells have been previously studied in 2D locomotion systems, with no specific role for septins in the motility of lymphocytes suggested to date (*13*, *17*). Thus, a punctuated pattern of septin striation in the "random-walk" migrating T cells, crawling on the flat 2D surfaces, and an elongation of T cell uropod with decreased random-walk efficiency, following knockdown of septin-7, have been reported (*13*). While the original report suggested that septins may participate in amoeboid motility, the early evidence had not resulted in the development of a causative mechanistic model over the following years. Consequently, our current data, such as identification of septin-positive cortical rings in migrating T cells and ECM-guided cortical partitioning, provide new mechanistic links that may help to clarify the reported correlation between the septins' expression (e.g., septin-7) and the amoeboid behavior of T cells (*13*).

Thus, we observe that primary human CD4$^+$ T cells compartmentalize their actomyosin cortex during amoeboid migration in response to steric cues, as demonstrated by ECM-guided formation of cortical rings. We identify septins in these rings and demonstrate that inhibition of septins' GTPase activity causes abrupt loss of cortical rings, cell segmentation, and transitioning to nonmigratory morphology. We confirm that migratory defects are also observed following the knockdown of septin-7. Together, our data suggest a nonstochastic mechanism of septin-mediated amoeboid motility for immune cells migrating within collagen gels. We propose that ECM-guided cell segmentation and segment-wise treadmilling of amoeboid cortex is an alternative yet complementary to both previously described mechanisms of amoeboid motility, i.e., blebbing and nonadhesive sliding of nonimmune melanoma cells (*41*, *42*). Moreover, multiple modes of amoeboid motility may indicate that processes of cortical blebbing, sliding, cortical deformations, and segment treadmilling can be the outcomes of the same amoeboid dynamics, depending on the cell microenvironment.

Briefly, the basis for sliding motility in amoeboid melanoma cells is a cortex treadmilling within the lasting leader bleb that powers friction-based cell displacement within an ideal "sandwich"-like microenvironment, i.e., between two confining parallel flat surfaces (*12*, *43*). Although the described sliding is considered a particular example of the wide and poorly characterized variety of amoeboid motility mechanisms, the locomotion based on friction seems energetically and mechanically suboptimal within more complex environments. Therefore, we question whether the observed compartmentalization of T cells in collagen gels indicates cell transitioning to a more optimized locomotion mechanism inherent to amoeboid immune cells in tissues. It is possible that the ECM-guided subdivision of the whole cell into a series of relatively independent contractile segments and their discrete treadmilling could allow hindrance-evasive peristaltic motility without friction-loaded displacement of the entire T cell cortex within a congested 3D microenvironment.

We propose the conjecture based on the observation of amoeboid sliding motility in nonimmune melanoma cells, where an excessive cross-linking of contractile cortical F-actin (e.g., by filamin-A and/or fascin), if combined with the cells' sterical confinement, results with cortex reorganization into a continuous system of coaxial circumferential fibers, forming an elongated cylindrical cortex of a leading bleb (*41*). We suggest that the reported filamin-A and/or fascin-rich circumferential cortical structures in melanoma cells and the observed discrete septin-positive cortical rings in human T cells are both analogous to the linear stress fibers. Moreover, both cortical structures and stress fibers depend, at least in part, on the scaffolding and stabilizing effects of septins (*20*, *36*, *44*). We support this idea demonstrating that septins may act as mechanosensitive F-actin cross-linkers, preferentially binding and stabilizing tensile actomyosin structures, as demonstrated by rapid dissociation of stress fibers and translocation of septins from actomyosin upon acute inhibition of either actomyosin contractility or septin GTPase activity. Therefore, similarly to stress fibers that condense from an isotropic actomyosin network into a load-resisting actomyosin band between anchoring focal adhesions (*45*, *46*), T cells may use septins to facilitate condensation of F-actin and α-actinin–rich cortical rings as a circularized (i.e., anchorless) form of the stress fiber in response to cortex indentation.

Moreover, we question whether the cross-linker–heavy but myosin-depleted cortical rings of T lymphocytes are noncontractile by design, preventing potential "cytokinesis-like" abscission of spheroid cell segments. It would be important to address the molecular mechanisms that may separate septin-based processes of actin cross-linking within noncontractile cortical F-actin rings in migrating T cells and more abundant contractile F-actin structures (*25*). Functionally, the nonstretchable cortical rings may serve to resist further stretching forces provided by myosin-rich contractile spheroid cell segments, e.g., by limiting "unsafe" levels of cortex-expanding hydrostatic pressure against surrounding steric obstacles. Thus, while mesenchymal cells use anchored myosin-rich stress fibers to enable the mechanosensing of the adhesive microenvironments, the nonadhesive amoeboid cells may use the anchorless myosin-depleted cortical rings for safe circumnavigation, i.e., obstacle avoidance, during the nonadhesive motility in sterically complex environments (*1*, *3*, *7*, *47*, *48*).

Please note that the observed architecture of septins and actomyosin in migrating T cells, as visualized by total NM2A, F-actin, septin-7, and phospho-myosin staining, is an imperfect biophysical indicator used in the absence of more appropriate methods for direct examination of 3D mechanics in migrating T cells, e.g., like high-speed atomic force microscopy suitable for measuring cells migrating within 3D collagen gels. However, following one of the overarching themes of biology that states that structure determines function, the architecture of actomyosin to some degree indicates differential mechanics of the adjacent cell compartments, based on the suggested feedback regulation between cell mechanics and actomyosin structures (*49*, *50*).

While our current capabilities to test the model more directly are technically limited, indirectly, our findings are consistent with the proposed model of segment-wise 3D amoeboid motility of T cells. Thus, as indirect evidence, we observe accumulation of septins in the segment-separating cortical rings and ECM-guided segmentation of actomyosin cytoskeleton. However, we also observe that amoeboid

migration depends on cortex contractility modulated by interplay of actomyosin and septins. These results suggest a dual role for septins that participate both in creating the cortical pressure by actomyosin cortex and in confining the pressure to orient its release via ECM-configured system of noncontractile cortical rings. While, at the current stage, it is not possible to separate cortical ring–associated (pressure orientation by ECM) and cortical segment–associated (pressure production) septin's roles in amoeboid migration, together, our findings complement the existing models of amoeboid motility yet suggest the contribution of relatively less studied septins.

In summary, our results suggest that T cells use septins for ECM-guided partitioning of actomyosin contractility, which could explain the previously reported links between amoeboid motility of T cells and septin-7 genetic knockdown (*13*, *17*). Specifically, we propose that cortex-indenting collagen fibers trigger septin accumulation and assembly of cross-linked F-actin rings within the actomyosin cortex, which restructures the spherical T cell into a hydrostatically unified system of expanding, static, and contracting cortical segments. Obstacle-evasive formation and treadmilling of cell segments provides continuous shape-changing dynamics and configures cortical forces (i.e., individual contractility of cell segments) to the preexisting spaces, locking cell on the confining collagen fibers and exerting forces sufficient enough for safe hindrance-evasive peristaltic propulsion of nucleus and cytoplasm through the series of narrow lumens in 3D microenvironments.

METHODS

Cell experiments

We maintained human MDA-MB-231 cells [American Type Culture Collection (ATCC) HTB-26] in Dulbecco's modified Eagle's medium (DMEM) with D-glucose (4.5 g/liter), L-glutamine, sodium pyruvate (110 mg/liter, Corning Cellgro, catalog no. 10013CV), and 10% heat-inactivated fetal bovine serum (FBS; HyClone, catalog no. SH30071.03H) at 37°C in 5% CO_2. Primary human $CD4^+$ T cells were isolated from commercially available whole human blood (STEMCELL Technologies Inc., USA, catalog no. 70507.1) with EasySep Human $CD4^+$ T Cell Isolation Kits (STEMCELL Technologies Inc., USA, catalog no. 17952), activated and expanded in ImmunoCult-XF T cell expansion medium (STEMCELL Technologies Inc., USA, catalog no. 10981) with the addition of ImmunoCult human CD3/CD28/CD2 T cell activator and human recombinant interleukin-2 (IL-2; STEMCELL Technologies Inc., USA), as per STEMCELL Technologies Inc. commercial protocol, at 37°C in 5% CO_2.

NK-92 cells (ATCC, CRL-2407) were cultured in the ImmunoCult-XF T cell expansion medium (STEMCELL Technologies Inc., USA) with the addition of human recombinant IL-2 (STEMCELL Technologies Inc., USA) and 10% heat-inactivated FBS (HyClone, catalog no. SH30071.03H) at 37°C in 5% CO_2. DO-11-10 cells (Sigma-Aldrich, catalog no. 85082301) were cultured in the ImmunoCult-XF T cell expansion medium (STEMCELL Technologies Inc., USA) with the addition of 5% heat-inactivated FBS (HyClone, catalog no. SH30071.03H) at 37°C in 5% CO_2. Primary mouse GFP-NM2A $CD4^+$ T cells were isolated from transgenic mice EasySep mouse $CD4^+$ T cell isolation kits (STEMCELL Technologies Inc., USA, catalog no. 19852), activated and expanded in ImmunoCult-XF T cell expansion medium (STEMCELL Technologies Inc., USA) with the addition of mouse CD3/CD28 T cell activator (Gibco, catalog no. 11452D) and mouse recombinant IL-2 (STEMCELL Technologies Inc., USA, catalog no. 78081.1), as per STEMCELL Technologies Inc. commercial protocol, at 37°C in 5% CO_2.

For experiments, all immune cells were treated in glass-bottom 35-mm petri dishes (MatTek Corp., catalog no. P35G-1.5-14-C) using DMSO (Sigma-Aldrich, catalog no. 472301), (−)−Blebbistatin enantiomer (Sigma-Aldrich, catalog no. 203391), nocodazole (Abcam, catalog no. ab120630), dynapyrazole A (Sigma-Aldrich, catalog no. SML2127), calyculin A (Sigma-Aldrich, catalog no. 208851), and septin inhibitor UR214-9 (synthesized by R.K.S.), as indicated in the main text. NK-92 cells were also studied using 5-μm Transwell permeable supports (Corning, catalog no. 3421) coated with human VCAM-1 (5 μg/ml; BioLegend, catalog no. 553706) at room temperature for 1 hour.

For transduction of DO-11-10 cells with shRNA against septin-7, we used MISSION shRNA lentiviral construct (pLKO.1-CMV-tGFP, Sigma-Aldrich, catalog no. TRCN0000101845) following the commercial protocol in ImmunoCult-XF T cell expansion medium with mouse recombinant IL-2. Five days after transduction, the cells were sorted for positive GFP expression. The GFP-positive cells and control cells were seeded in 1:1 ratio on top of collagen-I gels (STEMCELL Technologies Inc., catalog no. 07001) and allowed to migrate for 24 hours before fixation and staining. Transfection of MDA-MB-231 cells with pEGFP-C2_SEPT9_i1 (Addgene catalog no. 71609) and septin-7 (VectorBuilder, catalog no. VB220525-1339dzw) was performed in Opti-MEM (Gibco, catalog no. 31985-070) using SuperFect reagent (Qiagen, catalog no. 301307) according to the manufacturer's protocol.

Native electrophoresis and Western blot analysis

For cell lysate preparation, NK-92 cells were incubated with DMSO (Sigma-Aldrich, catalog no. 472301) or with 50 μM of septin's GTPase inhibitor UR214-9 for 3 hours in the cell culture incubator. After 3 hours, the cells were collected by centrifugation at 300*g* at 4°C for 5 min. Cell pellets were resuspended in 100 μl of the lysis buffer and prepared with 4× NativePAGE sample buffer (Invitrogen, catalog no. BN20032), 5% digitonin (Invitrogen, catalog no. BN2006), 10× cOmplete, Mini, EDTA-free protease inhibitor cocktail (Roche Diagnostics, catalog no. 11836170001), and sterile water. All reagents in the lysis buffer were prepared to 1×, and digitonin was prepared to 1%. Cell lysates were transferred to clean tubes and incubated on ice for 10 min. Following the incubation, the lysates were centrifuged at maximum speed (21,130*g*) at 4°C for 20 min to remove cell debris. The lysate supernatants were transferred to clean tubes, where 10 μl of 5 M NaCl was added to each 100 μl of lysates. The lysates were placed back on ice for 10 min and then additionally centrifuged at 21,130*g* at 4°C for 20 min. The collected lysate supernatants were then aliquoted and stored at −80°C until needed. To determine the protein concentration, a Pierce BCA protein assay kit was used (Thermo Fisher Scientific, catalog no. 23227).

Native gel electrophoresis was performed using NativePAGE 3 to 12%, bis-tris, 1.0 mm, mini protein gels (Invitrogen, catalog no. BN1001BOX) followed by the NativePAGE bis-tris mini gel electrophoresis protocol. For loading, we used 5 μl of NativeMark unstained protein standard (Invitrogen, catalog no. LC0725) and 5 μg of each sample. After running, the gel was placed in 2× NuPAGE transfer buffer (20×) (Invitrogen, catalog no. NP0006) for 10 min and then transferred to a polyvinylidene difluoride (PVDF) membrane with the iBlot 2 Transfer Stacks, PVDF, mini (Invitrogen, catalog no. IB24002) on an iBlot 2 Gel Transfer Device (following proposed Method P3).

The membrane was then incubated with 8% acetic acid for 10 min, rinsed, and air-dried overnight at room temperature.

The membrane was reactivated with methanol and then blocked in Intercept tris-buffered saline (TBS) blocking buffer (LI-COR, catalog no. 927-60001) for 4 hours, shaking at room temperature. After blocking, the membrane was incubated with rabbit α-human septin-7 antibody (1:1000, Immuno-Biological Laboratories, catalog no. 18991) overnight at 4°C, shaking. The antibodies were diluted with Intercept antibody diluent T20 TBS (LI-COR, catalog no. 927-65001). After overnight incubation, the membranes were washed with TBS and 0.05% Tween. Next, the membranes were incubated for 1 hour at room temperature, shaking, with IRDye 800CW goat anti-rabbit secondary antibody (1:5000, LI-COR, catalog no. 926-32211). All antibodies were diluted with the Intercept antibody diluent T20 TBS. Following the incubation, the membranes were again washed with TBS and 0.05% Tween. The membranes were then imaged on a LI-COR Odyssey CLx and analyzed via ImageStudio (version 5.2).

Polymerization of prestained collagen gels

To prepare collagen-I gel (3 mg/ml), we assembled a gel premix on ice in a prechilled Eppendorf tube. To 1 volume of CellAdhere type I bovine (6 mg/ml, STEMCELL Technologies Inc., USA), we added $^{8}/_{10}$ volume of DMEM, $^{1}/_{10}$ volume of 10× phosphate-buffered saline (PBS), $^{1}/_{20}$ volume of 1 M Hepes, and $^{1}/_{20}$ volume of 1 M Atto 647 *N*-hydroxysuccinimide ester (Sigma-Aldrich), Alexa Fluor 568 ester (Molecular Probes, catalog no. A20003), or Alexa Fluor 488 ester (Molecular Probes, catalog no. A20000). A drop of premixed gel (~50 μl) was spread immediately on a glass surface of a plasma-treated glass-bottom 35-mm petri dish (MatTek Corp., catalog no. P35G-1.5-14-C) with a pipette tip. During polymerization (room temperature, for overnight), gels were covered with 1 ml of mineral oil (Sigma-Aldrich, catalog no. M8410) to prevent evaporation of water. Before adding T cells, polymerized gels were rinsed with PBS to remove the unpolymerized gel components.

Synthesis of UR214-9

Equimolar mixture of 3-amino-2-fluorobenzotrifluoride (Combi-Blocks, catalog no.QA-4188) and 2,6-dichloro-4-isocyanatopyridine (Toronto Research Chemicals, catalog no.159178-03-7) was stirred and heated in anhydrous Toluene at 85°C overnight. The separated UR214-9 was filtered and dried under vacuum in a desiccator. A portion of UR214-9 was detected in the Toluene layer, which was concentrated and purified by thin-layer chromatography using ethyl acetate and hexane as eluents. The pure product band was scrapped off the glass plate, and UR214-9 was stripped from the silica gel using dichloromethane + MeOH through a sintered funnel. The solvent was evaporated using a Buchi rotary evaporator to obtain UR214-9 as an off-white powder. The structure was confirmed by x-ray crystallography.

Super-resolution and epifluorescent microscopy

For imaging, fixed cell samples were immunostained as indicated in corresponding figures. Super-resolution imaging was performed using an Instant structured illumination microscopy (iSIM) system (VisiTech Intl, Sunderland, UK) equipped with an Olympus UPLAPO-HR ×100/1.5 NA objective. Image acquisition and system control was done using MetaMorph Premiere software (Molecular Devices LLC, San Jose, CA). Images were deconvolved with an iSIM-specific commercial plugin from Microvolution (Cupertino, CA) in FIJI. Live cell imaging microscopy experiments were performed on epifluorescent Leica DMi8 AFC microscope (Leica, Germany) equipped with a temperature (37°C)–, CO_2 (5%)–, and humidity-controlled chamber (OkoLab, Italy) at ×20, ×40, and ×63 magnifications. All analyses were performed automatically and/or manually using Leica LAS X software (Leica, Germany) and the ImageJ/FIJI. Figures were composed using unmodified LAS X–generated TIFF images with Adobe Illustrator CC 2021 (Adobe).

For iSIM, we fixed cells with 4% paraformaldehyde (PFA; Sigma-Aldrich, catalog no. P6148) for the duration of 30 min at room temperature. PFA-fixed cells were then rinsed with 1% bovine serum albumin (BSA) in PBS, followed by 60-min-long blocking with 1% BSA (Thermo Fisher Scientific, catalog no. BP9704) in PBS (Thermo Fisher Scientific, catalog no.10010023). For immunofluorescence staining, all primary antibodies were diluted in 1% BSA PBS. The duration of the incubation with any of the listed primary antibody solutions was 2 hours at room temperature. Similarly, labelings with Alexa Fluor–conjugated secondary antibodies (Thermo Fisher Scientific) were performed at their final concentration of 5 μg/ml for the duration of 1 hour in 1% BSA PBS at room temperature. After washing out the excess secondary antibodies, chromatin and actin, if necessary, were labeled with 1:1000 Hoechst solution (Tocris, catalog no.5117) and SiR-actin (Cytoskeleton Inc., catalog no. CY-SC001) or phalloidin conjugates (Sigma-Aldrich, catalog no. 49409, Thermo Fisher Scientific, catalog no. A12380), respectively. We mounted samples using 90% glycerol (Sigma-Aldrich, catalog no. G5516) in 1× PBS.

Automated detection and tracking of cells in collagen matrix

The detection of individual cell tracks and speeds in phase-contrast time-lapse images was performed with the following steps: (i) correction of the background illumination, (ii) detection of cell edges, (iii) rescaling and applying masks, (iv) watershed segmentation, (v) tracking, and (vi) filtering noise and correction for trajectory fragmentations. The following steps allow us the detection of individual cell tracks and speeds in phase-contrast time-lapse images. First, the variation of the background illumination across each image was corrected by subtracting the image smoothed by the Gaussian filter (with an SD of 10 pixels) from the original image. Second, the resulting background-corrected images were processed with the local SD filter (with the 9 × 9–pixel neighborhood matrix) to highlight cell edge regions. Third, the resulting SD maps were smoothed by the Gaussian filter (with an SD of 5) to obtain the grayscale representation of cells. Next, the resulting images were rescaled with a log function and masked with a threshold value of 6.4. To identify individual cells, the resulting binary masks were overlaid with the smoothed SD maps and subjected to our in-house watershed segmentation routine [using an algorithm that includes "draining" criteria allowing to avoid over-segmentation (*51*), which is typical for the traditional watershed approaches]. Centroids of all eight-connected objects in the segmented images were recorded for tracking.

The tracking of cell centroids was performed on the basis of minimal distance matching in consecutive time frames (within the radius of 40 pixels). The tracking pipeline includes the following steps. If two or more trajectories meet (e.g., one of the cells moves over or under another cell in the 3D matrix), the new position is added to the longest up to the time point track while the other one(s) ends. If a trajectory splits (e.g., another cell moves into the focus plane from above or below the tracked cell in the 3D matrix), the nearest new

position is added to the current track, while the other new position starts a new track. Because cells move in the 3D environment, it is possible for cells to come in and out of the focus plane, which leads to recording several shorter tracks of the same cell. Since we do not use trajectory length as a phenotype characteristic, the occasional fragmentation of trajectories does not affect our analysis. However, it is also possible that a cell migrates at the border of the focus plane, repeatedly coming in and out of focus (i.e., flickering) and creating multiple ultrashort tracks. To reduce such disruptions of individual cell tracks, we apply a "flickering correction" algorithm (*52*) that detects colocalization of the end of one trajectory (x_e,y_e) at time t and the beginning of another trajectory (x_b,y_b) at time $t + 2$ and merge these trajectories into one by assigning cell position at $[(x_e + x_b)/2, (y_e + y_b)/2]$ at time $t + 1$. Because we track cells with complex (ball-chain) shapes, it is possible for our detection algorithm to identify more than one compartment of the same cell as separate cells. As a result, a single cell may produce several nearly colocalized trajectories. To avoid a potential bias due to such double counting, we apply a "cloning correction" algorithm that detects each trajectory remaining in the vicinity of another longer trajectory for the whole duration of this shorter track and removes such tracks from the record. Last, we remove all the "tracks" of immobilized debris in the image by disregarding trajectories that remain within the detection radius (40 pixels) for the entire track duration.

Mean squared displacement (MSD) is calculated as the average of the squared values across the entire imaged cell population and is defined as the linear distance between a current T cell position (t_i) and its initial position on the track $(t_0 = 0)$. Displacement ratio is calculated as the population-wide average value of the ratios of the linear distance between the T cell position at time t and its initial position on the track to the distance that T cell has traveled along its curved track up to time t. Thus, if a cell moving strictly along a line would have the displacement ratio of one, a cell wandering around its initial location would have the displacement ratio close to zero. Thus, displacement ratio is a metric of directional persistence. Diffusion exponent is the slope of the linear fit to MSD in log-log scale. Note that for a particle undergoing Brownian motion in 3D, $MSD = 6Dt$, where D is the diffusion constant. More generally, MSD can be approximated as $MSD \sim t^a$, so that in log-log scale, we have approximately linear dependence: $\log(MSD) = a\log(t) + \text{constant}$, where a is the diffusion exponent. Thus, the diffusion exponent is a metric of the deviation of cell trajectories from the normal Brownian motion (superdiffusion/active transport for $a > 1$ and subdiffusion for $a < 1$).

Quantification of the colocalization of F-actin, collagen-1, and septin-7 rings

The pipeline for measuring relative distances between the highest-intensity ring planes in F-actin, collagen-1, and septin-7 channels includes the following steps. First, the z-stack images are resampled using linear interpolation to convert 0.065 × 0.065 × 0.200 μm data grid to the isometric grid with 0.065 × 0.065 × 0.065 μm voxels.

Next, the data are subjected to 3D rotation to align the plane of the ring with one of the coordinate-system planes: *xy*, *xz*, or *yz*. The rotation is performed in two steps: (i) around one of the axes to achieve linear rather than elliptical projection of the ring on a coordinate-system plane and (ii) around another axis to align the axis of the ring with the horizontal or vertical direction. The same rotation is applied to all three channels; however, the alignments are made using the F-actin channel that has the highest signal-to-noise ratio. Such alignment allows for analyzing signals in the plane moving along the ring axis sequentially with 0.065-μm step (scanning plane in Fig. 6, A to C, and movie S4).

Next, we evaluate the overlap between F-actin and collagen-1, F-actin and septin-7, and collagen-1 and septin-7 as functions of the scanning plane position. Figure 6B illustrates the signal in each channel when the scanning plan passes the central part of the F-actin ring. The measure of intensity overlap (Fig. 6D) for two channels, ch1 and ch2, as a function of the scanning plane position, p, is defined here as

$$C_{\mathrm{ch1,ch2}}(p) = \Sigma_{i,j\in\Omega} I_{\mathrm{ch1}}(p) \times I_{\mathrm{ch2}}(p)$$

where Ω is the binary mask of the actin channel at the plane with maximal F-actin signal. Thus, the summation is performed over scanning plane pixels i,j with $\Omega = 1$. The plane position of the maximal F-actin signal, the threshold value defining mask, and the two rotation angles are adjustable parameters of the pipeline.

Last, the relative distances between the highest intensity planes of the F-actin, collagen-1, and septin-7 rings are determined as the distances between the peaks of the corresponding overlaps

$$\Delta_{\mathrm{ch1,ch2}} = \mathrm{abs}\left[\arg\max_p C_{\mathrm{ch1,ch3}}(p) - \arg\max_p C_{\mathrm{ch2,ch3}}(p)\right]$$

All the steps of this pipeline were programmed using the MATLAB platform. Applying this analysis to nine rings consistently show the same result (Fig. 6E) that the peaks of intensity in the planes of the ring are coaligned for F-actin and septin-7 (~0.065 μm, i.e., at the borderline of the image resolution) and shifted for F-actin and collagen-1 (0.26 μm, i.e., ~5% of the ring diameter).

Computational modeling

Crystal structure of the human septin-7 GTPase domain was downloaded from the Protein Data Bank (PDB entry: 3TW4). The ligand (UR214-9 and FCF) was converted into an SDF file via a conversion tool available at https://datascience.unm.edu/tomcat/biocomp/convert. Protein preparation was handled by neurosnap.ai DiffDock tool (*53*). Neurosnap (*54*) cleans up the structure when the structure is uploaded. Some of the preparatory steps that neurosnap accomplishes are ligand removal, protonation of protein, and assigning charges. Docking was performed by diffdock hosted on neurosnap.ai[2]. One hundred iterations were run. The highest confidence (rank) pose selected for both FCF and UR214-9 was visualized via Discovery studio visualizer. Images were generated by discovery studio visualizer (*55*). Binding energy was computed via Kdeep, a neural network for calculating binding energies [K_{DEEP}: protein-ligand absolute binding affinity prediction via 3D-convolutional neural networks (*56*) found on Playmolecule (https://playmolecule.com/Kdeep/)]. Ligand and protein were uploaded, and the job was submitted. The Kdeep model was set to default, and the classifier was set to bindscope. Binding energies were obtained as kcal/mol units std.qaqw.

Statistical analysis

Only pairwise comparisons as one-sided t tests between a control group and all other conditions are used to analyze the data, as well as between paired −Blebbistatin and +Blebbistatin cotreatment groups. Statistical analysis is performed using either KaleidaGraph 5

for MacOS (Synergy Software) or Prism 7b (GraphPad Software Inc.). The exact P values are indicated on the plots, unless $P < 0.0001$, i.e., below the cutoff lower limit for KaleidaGraph and Prism software. Sample size n for each comparison is reported in the corresponding plots (i.e., n reflects the number of measured individual cells). Number of replicates is three, unless specified otherwise. Data are shown as box-and-whisker diagrams: first quartile, median, third quartile, and 95% confidence interval.

Supplementary Materials

The PDF file includes:
Supplementary Methods
Figs. S1 to S6
Table S1
Legends for movies S1 to S6

Other Supplementary Material for this manuscript includes the following:
Movies S1 to S6

REFERENCES AND NOTES

1. A. Reversat, F. Gaertner, J. Merrin, J. Stopp, S. Tasciyan, J. Aguilera, I. de Vries, R. Hauschild, M. Hons, M. Piel, A. Callan-Jones, R. Voituriez, M. Sixt, Cellular locomotion using environmental topography. *Nature* **582**, 582–585 (2020).
2. Z. Sadjadi, R. Zhao, M. Hoth, B. Qu, H. Rieger, Migration of cytotoxic T lymphocytes in 3D collagen matrices. *Biophys. J.* **119**, 2141–2152 (2020).
3. K. Wolf, R. Müller, S. Borgmann, E.-B. Bröcker, P. Friedl, Amoeboid shape change and contact guidance: T-lymphocyte crawling through fibrillar collagen is independent of matrix remodeling by MMPs and other proteases. *Blood* **102**, 3262–3269 (2003).
4. A. Takesono, S. J. Heasman, B. Wojciak-Stothard, R. Garg, A. J. Ridley, Microtubules regulate migratory polarity through Rho/ROCK signaling in T cells. *PLOS One* **5**, e8774 (2010).
5. E. D. Tabdanov, N. J. Rodríguez-Merced, A. X. Cartagena-Rivera, V. V. Puram, M. K. Callaway, E. A. Ensminger, E. J. Pomeroy, K. Yamamoto, W. S. Lahr, B. R. Webber, B. S. Moriarity, A. S. Zhovmer, P. P. Provenzano, Engineering T cells to enhance 3D migration through structurally and mechanically complex tumor microenvironments. *Nat. Commun.* **12**, 2815 (2021).
6. M. F. Krummel, R. S. Friedman, J. Jacobelli, Modes and mechanisms of T cell motility: Roles for confinement and myosin-IIA. *Curr. Opin. Cell Biol.* **30**, 9–16 (2014).
7. G. Charras, E. Paluch, Blebs lead the way: How to migrate without lamellipodia. *Nat. Rev. Mol. Cell Biol.* **9**, 730–736 (2008).
8. G. T. Charras, J. C. Yarrow, M. A. Horton, L. Mahadevan, T. J. Mitchison, Non-equilibration of hydrostatic pressure in blebbing cells. *Nature* **435**, 365–369 (2005).
9. G. T. Charras, C.-K. Hu, M. Coughlin, T. J. Mitchison, Reassembly of contractile actin cortex in cell blebs. *J. Cell Biol.* **175**, 477–490 (2006).
10. M. Fritzsche, A. Lewalle, T. Duke, K. Kruse, G. Charras, Analysis of turnover dynamics of the submembranous actin cortex. *Mol. Biol. Cell* **24**, 757–767 (2013).
11. J. Renkawitz, K. Schumann, M. Weber, T. Lämmermann, H. Pflicke, M. Piel, J. Polleux, J. P. Spatz, M. Sixt, Adaptive force transmission in amoeboid cell migration. *Nat. Cell Biol.* **11**, 1438–1443 (2009).
12. G. Adams Jr., M. Preciado-Lopez, R. S. Fischer, M. A. Baird, J. Logue, C. M. Waterman, Functional behavior of melanoma cells under high confinement, high contractility and low adhesion mediating leader bleb based motility. *Mol. Biol. Cell* **29** (2018).
13. A. J. Tooley, J. Gilden, J. Jacobelli, P. Beemiller, W. S. Trimble, M. Kinoshita, M. F. Krummel, Amoeboid T lymphocytes require the septin cytoskeleton for cortical integrity and persistent motility. *Nat. Cell Biol.* **11**, 17–26 (2009).
14. A. I. Ivanov, H. T. Le, N. G. Naydenov, F. Rieder, Novel functions of the septin cytoskeleton: Shaping up tissue inflammation and fibrosis. *Am. J. Pathol.* **191**, 40–51 (2021).
15. R. Nishihama, M. Onishi, J. R. Pringle, New insights into the phylogenetic distribution and evolutionary origins of the septins. *Biol. Chem.* **392**, 681–687 (2011).
16. S. Mostowy, P. Cossart, Septins: The fourth component of the cytoskeleton. *Nat. Rev. Mol. Cell Biol.* **13**, 183–194 (2012).
17. J. K. Gilden, S. Peck, Y.-C. M. Chen, M. F. Krummel, The septin cytoskeleton facilitates membrane retraction during motility and blebbing. *J. Cell Biol.* **196**, 103–114 (2012).
18. B. L. Woods, A. S. Gladfelter, The state of the septin cytoskeleton from assembly to function. *Curr. Opin. Cell Biol.* **68**, 105–112 (2021).
19. E. T. Spiliotis, Spatial effects—Site-specific regulation of actin and microtubule organization by septin GTPases. *J. Cell Sci.* **131**, jcs207555 (2018).
20. L. Dolat, J. L. Hunyara, J. R. Bowen, E. P. Karasmanis, M. Elgawly, V. E. Galkin, E. T. Spiliotis, Septins promote stress fiber–mediated maturation of focal adhesions and renal epithelial motility. *J. Cell Biol.* **207**, 225–235 (2014).
21. K. Schmidt, B. J. Nichols, Functional interdependence between septin and actin cytoskeleton. *BMC Cell Biol.* **5**, 43 (2004).
22. E. T. Spiliotis, K. Nakos, Cellular functions of actin- and microtubule-associated septins. *Curr. Biol.* **31**, R651–R666 (2021).
23. N. Founounou, N. Loyer, R. Le Borgne, Septins regulate the contractility of the actomyosin ring to enable adherens junction remodeling during cytokinesis of epithelial cells. *Dev. Cell* **24**, 242–255 (2013).
24. M. Kinoshita, C. M. Field, M. L. Coughlin, A. F. Straight, T. J. Mitchison, Self- and actin-templated assembly of mammalian septins. *Dev. Cell* **3**, 791–802 (2002).
25. M. Mavrakis, Y. Azou-Gros, F.-C. Tsai, J. Alvarado, A. Bertin, F. Iv, A. Kress, S. Brasselet, G. H. Koenderink, T. Lecuit, Septins promote F-actin ring formation by crosslinking actin filaments into curved bundles. *Nat. Cell Biol.* **16**, 322–334 (2014).
26. M. P. Estey, C. Di Ciano-Oliveira, C. D. Froese, M. T. Bejide, W. S. Trimble, Distinct roles of septins in cytokinesis: SEPT9 mediates midbody abscission. *J. Cell Biol.* **191**, 741–749 (2010).
27. O. Lieleg, K. M. Schmoller, M. M. A. E. Claessens, A. R. Bausch, Cytoskeletal polymer networks: Viscoelastic properties are determined by the microscopic interaction potential of cross-links. *Biophys. J.* **96**, 4725–4732 (2009).
28. Y. Oh, E. Bi, Septin structure and function in yeast and beyond. *Trends Cell Biol.* **21**, 141–148 (2011).
29. A. A. Bridges, A. S. Gladfelter, Septin form and function at the cell cortex. *J. Biol. Chem.* **290**, 17173–17180 (2015).
30. A. S. Zhovmer, A. Manning, C. Smith, J. B. Hayes, D. T. Burnette, J. Wang, A. X. Cartagena-Rivera, N. V. Dokholyan, R. K. Singh, E. D. Tabdanov, Mechanical counterbalance of kinesin and dynein motors in a microtubular network regulates cell mechanics, 3D architecture, and mechanosensing. *ACS Nano* **15**, 17528–17548 (2021).
31. K. K. Kim, R. K. Singh, N. Khazan, A. Kodza, N. A. Singh, A. Jones, U. Sivagnanalingam, M. Towner, H. Itamochi, R. Turner, R. G. Moore, Development of potent Forchlorfenuron analogs and their cytotoxic effect in cancer cell lines. *Sci. Rep.* **10**, 3241 (2020).
32. M. Krendel, F. T. Zenke, G. M. Bokoch, Nucleotide exchange factor GEF-H1 mediates cross-talk between microtubules and the actin cytoskeleton. *Nat. Cell Biol.* **4**, 294–301 (2002).
33. Q. Hu, W. J. Nelson, E. T. Spiliotis, Forchlorfenuron alters mammalian septin assembly, organization, and dynamics. *J. Biol. Chem.* **283**, 29563–29571 (2008).
34. R. K. Singh, K. K. Kim, N. Khazan, R. B. Rowswell-Turner, C. Laggner, A. Jones, P. Srivastava, V. Hovanesian, L. Lamere, T. Conley, R. Pandita, C. Baker, J. R. Myers, E. Pritchett, A. Ahmad, L. Ruffolo, K. Jackson, S. A. Gerber, J. Ashton, M. T. Milano, D. Linehan, R. G. Moore, Septins disruption controls tumor growth and enhances efficacy of Herceptin. *Cold Spring Harb. Perspect. Biol.*, (2020).
35. T. H. Cheffings, N. J. Burroughs, M. K. Balasubramanian, Actomyosin ring formation and tension generation in eukaryotic cytokinesis. *Curr. Biol.* **26**, R719–R737 (2016).
36. J. Salameh, I. Cantaloube, B. Benoit, C. Poüs, A. Baillet, Cdc42 and its BORG2 and BORG3 effectors control the subcellular localization of septins between actin stress fibers and microtubules. *Curr. Biol.* **31**, 4088–4103.e5 (2021).
37. A. Füchtbauer, L. B. Lassen, A. B. Jensen, J. Howard, A. de S. Quiroga, S. Warming, A. B. Sørensen, F. S. Pedersen, E.-M. Füchtbauer, Septin9 is involved in septin filament formation and cellular stability. *Biol. Chem.* **392**, 769–777 (2011).
38. A. Beber, C. Taveneau, M. Nania, F.-C. Tsai, A. Di Cicco, P. Bassereau, D. Lévy, J. T. Cabral, H. Isambert, S. Mangenot, A. Bertin, Membrane reshaping by micrometric curvature sensitive septin filaments. *Nat. Commun.* **10**, 420 (2019).
39. Y. F. Dagdas, K. Yoshino, G. Dagdas, L. S. Ryder, E. Bielska, G. Steinberg, N. J. Talbot, Septin-mediated plant cell invasion by the rice blast fungus, *Magnaporthe oryzae*. *Science* **336**, 1590–1595 (2012).
40. V. Ruprecht, S. Wieser, A. Callan-Jones, M. Smutny, H. Morita, K. Sako, V. Barone, M. Ritsch-Marte, M. Sixt, R. Voituriez, C.-P. Heisenberg, Cortical contractility triggers a stochastic switch to fast amoeboid cell motility. *Cell* **160**, 673–685 (2015).
41. G. Adams Jr., M. P. López, A. X. Cartagena-Rivera, C. M. Waterman, Survey of cancer cell anatomy in nonadhesive confinement reveals a role for filamin-A and fascin-1 in leader bleb-based migration. *Mol. Biol. Cell* **32**, 1772–1791 (2021).
42. J. S. Logue, A. X. Cartagena-Rivera, M. A. Baird, M. W. Davidson, R. S. Chadwick, C. M. Waterman, Erk regulation of actin capping and bundling by Eps8 promotes cortex tension and leader bleb-based migration. *eLife* **4**, e08314 (2015).
43. Y.-J. Liu, M. Le Berre, F. Lautenschlaeger, P. Maiuri, A. Callan-Jones, M. Heuzé, T. Takaki, R. Voituriez, M. Piel, Confinement and low adhesion induce fast amoeboid migration of slow mesenchymal cells. *Cell* **160**, 659–672 (2015).
44. B. E. Kremer, L. A. Adang, I. G. Macara, Septins regulate actin organization and cell-cycle arrest through nuclear accumulation of NCK mediated by SOCS7. *Cell* **130**, 837–850 (2007).

45. J. I. Lehtimäki, E. K. Rajakylä, S. Tojkander, P. Lappalainen, Generation of stress fibers through myosin-driven reorganization of the actin cortex. *eLife* **10**, e60710 (2021).
46. T. Vignaud, C. Copos, C. Leterrier, M. Toro-Nahuelpan, Q. Tseng, J. Mahamid, L. Blanchoin, A. Mogilner, M. Théry, L. Kurzawa, Stress fibres are embedded in a contractile cortical network. *Nat. Mater.* **20**, 410–420 (2021).
47. E. Paluch, M. Piel, J. Prost, M. Bornens, C. Sykes, Cortical actomyosin breakage triggers shape oscillations in cells and cell fragments. *Biophys. J.* **89**, 724–733 (2005).
48. J. van der Gucht, E. Paluch, J. Plastino, C. Sykes, Stress release drives symmetry breaking for actin-based movement. *Proc. Natl. Acad. Sci. U.S.A.* **102**, 7847–7852 (2005).
49. R. Fernandez-Gonzalez, J. A. Zallen, Cell mechanics and feedback regulation of actomyosin networks. *Sci. Signal.* **2**, pe78 (2009).
50. R. Sakamoto, D. S. Banerjee, V. Yadav, S. Chen, M. L. Gardel, C. Sykes, S. Banerjee, M. P. Murrell, Membrane tension induces F-actin reorganization and flow in a biomimetic model cortex. *Commun. Biol.* **6**, 325 (2023).
51. S. Hladyshau, M. Kho, S. Nie, D. Tsygankov, Spatiotemporal development of coexisting wave domains of Rho activity in the cell cortex. *Sci. Rep.* **11**, 19512 (2021).
52. D. Tsygankov, C. G. Bilancia, E. A. Vitriol, K. M. Hahn, M. Peifer, T. C. Elston, CellGeo: A computational platform for the analysis of shape changes in cells with complex geometries. *J. Cell Biol.* **204**, 443–460 (2014).
53. G. Corso, H. Stärk, B. Jing, R. Barzilay, T. Jaakkola, DiffDock: Diffusion steps, twists, and turns for molecular docking. arXiv:2210.01776 [q-bio.BM] (2022).
54. Neurosnap Inc. Accelerate your research with the latest in computational biology. https://neurosnap.ai/.
55. D. S. Biovia, Discovery Studio Visualizer (2019).
56. J. Jiménez, M. Škalič, G. Martínez-Rosell, G. De Fabritiis, K_{DEEP}: Protein–ligand absolute binding affinity prediction via 3D-convolutional neural networks. *J. Chem. Inf. Model.* **58**, 287–296 (2018).

Acknowledgments: We thank C. Combs and D. Malide for the Light Microscopy Core support at the National Heart, Lung, and Blood Institute, NIH. **Funding:** E.D.T. and this work were supported by the Department of Pharmacology, Penn State College of Medicine via the startup funds. D.T. is supported by the National Science Foundation (CMMI 1942561) and the National Institutes of Health (R01GM136892). A.S.Z., X.M., A.N., O.P., and A.M. were supported by the FDA Intramural Research Program of the Center for Biologics Evaluation and Research. A.X.C.-R. and C.S. were supported by the National Institutes of Health (NIH) Intramural Research Program in the National Institute of Biomedical Imaging and Bioengineering (NIH grant no. ZIA EB000094) and by the NIH Distinguished Scholars Program. P.J.S. received the support of Human Frontier Science Program (HFSP) RGP 0032/2022 and Forschungszentrum Medizintechnik Hamburg (FMTHH, grant 04fmthh2021). **Author contributions:** Conceptualization: E.D.T. and A.S.Z. Data curation: E.D.T. and A.S.Z. Investigation: E.D.T., A.S.Z., A.M., C.S., A.N., O.P., P.J.S., X.M., D.T., A.X.C.-R., N.A.S., and R.K.S. Methodology: E.D.T. and A.S.Z. designed and microfabricated mechanobiological platforms. D.T. and A.X.C.-R. provided live cell behavior study methods. A.M., C.S., and A.X.C.-R. provided live cell mechanobiology methods. D.T. provided advanced methods for cell structural dynamics analysis. D.T. and P.J.S. provided automated cell migration analysis methods. N.A.S. performed in silico molecular modeling of UR214-9 docking to septin. Formal analysis: E.D.T., A.S.Z., D.T., P.J.S., A.M., C.S., A.N., O.P., and X.M. Resources: A.S.Z. provided super-resolution microscopy access and primary murine T cells. R.K.S. designed, synthesized, purified, chemically tested, and verified mammalian septin inhibitor UR214-9. Software: D.T. and P.J.S. designed scripts for automated and manual cell structural dynamics analysis. Visualization: A.S.Z., E.D.T., and D.T. Writing: E.D.T. and A.S.Z. Supervision: E.D.T. **Competing interests:** The authors declare that they have no competing interests. **Data and materials availability:** The UR214-9 septin GTPase inhibitor compound can be provided by R.K.S. pending scientific review and a completed material transfer agreement. Requests for the UR214-9 should be submitted to: Rakesh_Singh@URMC.Rochester.edu. All data needed to evaluate the conclusions in the paper are present in the paper and/or the Supplementary Materials. Raw source data, tabulated measurements, and used scripts are available at Ms. No. adi1788 source files at Dryad: https://doi.org/10.5061/dryad.m905qfv7g.

Submitted 7 April 2023
Accepted 1 December 2023
Published 3 January 2024
10.1126/sciadv.adi1788